Bachelor’s Thesis

Simulations and measurements of angular selective electron transmission and detection for the KATRIN experiment

Tim König

Münster, 26.07.2021

Advisor Prof. Dr. Christian Weinheimer

Second advisor Prof. Dr. Alfons Khoukaz

Contents

1 Introduction

First proposed in 1930 by Wolfgang Pauli, the neutrino is meanwhile an acknowledged part of the Standard Model of particle physics (SM) and an important research field. While the absolute neutrino mass was considered to be zero for a long time, experiments like the Sudbury Neutrino Observatory or the Super-Kamiokande have proven neutrino oscillations that are the evidence for a neutrino mass greater than zero. Since neutrino oscillation experiments allow only the observation of squared mass splittings, alternative approaches are necessary to determine the absolute neutrino mass [1]. Unlike cosmological studies, which are highly model-dependent and neutrinoless double-beta decay experiments, the KArlsruhe TRItium Neutrino experiment (KATRIN) poses a direct way of neutrino mass measurement. Thus, the KATRIN experiment is designed to measure the neutrino mass with a sensitivity of $0.2\,\mathrm{eV}$ (at $90\,\%$ C.L.). To reach the sensitivity goal KATRIN requires high statistics, excellent energy resolution and very low background level [2] [1].

In this work we investigate the background suppression capabilities of a candidate, called active Transverse Energy Filter (aTEF), that is possibly able to reduce most of the remaining background of the KATRIN experiment. The aim of this thesis is a verification of the proposed background mitigation concept.

2 Kinematic neutrino mass measurements

This chapter gives a short introduction to the KATRIN experiment. It focuses on the Magnetic Adiabatic Collimation with Electrostatic (MAC-E) filter concept in order to explain, how the the beta-spectra of the tritium decay is recorded. As this work deals with a method of KATRIN background suppression, this background is characterised, before several mitigation concepts are discussed.

2.1 The KATRIN experiment

The KATRIN experiment aims to measure the average electron neutrino mass $m_{\bar{\nu}}$ with a sensitivity of $0.2\,\mathrm{eV/c^2}$ at $90\,\%$ confidence level (C.L.). The kinematic measurements of the tritium ($^3_1$H) beta-decay, displayed here in atomic form [3],

$$^3_1\mathrm{H} \rightarrow {}^3_2\mathrm{He}^+ + e^- + \bar{\nu}_e \tag{2.1}$$

represent a model independent way of measuring the neutrino mass. The squared effective anti-neutrino mass $m_{\bar{\nu}_e}$, consisting of the incoherent sum of the three mass eigenstates $m\left(\nu_i\right)$ and the neutrino matrix element U_{ei} [4],

$$m_{\bar{\nu}_e}^2 = \sum \left|U_{\mathrm{ei}}\right|^2 m\left(\nu_i\right)^2 \tag{2.2}$$

can directly be obtained by measuring the energy spectra of the well known β-decay, described by the Fermi theory [5]:

$$\frac{dN}{dE_{\mathrm{kin}}} \propto p\left(E_{\mathrm{kin}} + m_e c^2\right)\left(E_0 - E_{\mathrm{kin}}\right)\sqrt{\left(E_0 - E_{\mathrm{kin}}\right)^2 - m_{\bar{\nu}_e}^2 c^4}. \tag{2.3}$$

Mainly the endpoint region around $18.6\,\mathrm{keV}$ of the energy spectra is sensitive to squared neutrino mass $m_{\bar{\nu}_e}^2$ measurements (see Fig. 2.1).
After the second measurement campaign in 2019, first sub-eV upper limits on the neutrino mass were published 2021 reaching a sensitivity of $0.7\,\mathrm{eV}$ [7].

$$m_{\bar{\nu}_e} < 0.8\mathrm{eV}c^{-2} \quad (90\%\ \text{C.L.}\ ) \tag{2.4}$$

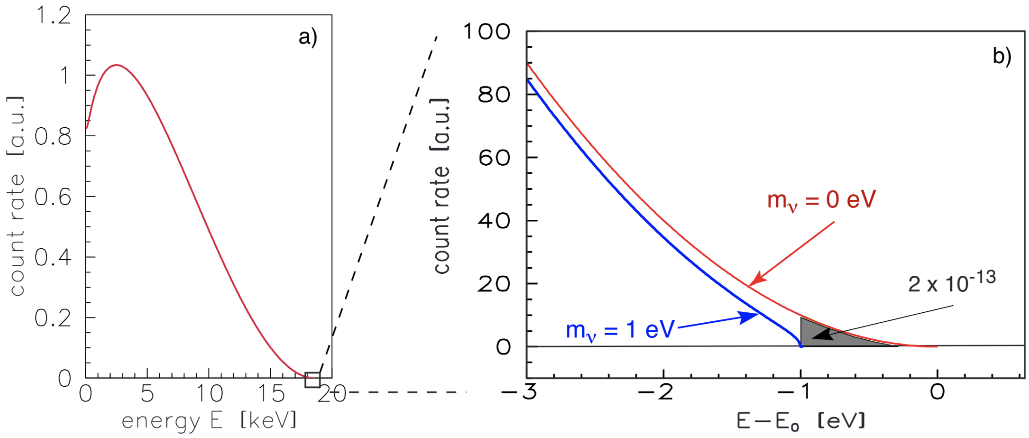

Figure 2.1.: The tritium beta-decay energy spectra in **a)** full range and **b)** at the endpoint region, modelled for a neutrino mass $m_{\bar{\nu}_e}$ of $1\,\mathrm{eV}$ and $0\,\mathrm{eV}$. At the endpoint the neutrino is generated at rest, so that all kinetic energy is transferred to the electron. Then just the neutrino rest mass is missing and for this case can be read directly from the offset difference. One drawback is the amount of these endpoint decays, which accounts for only $2 \cdot 10^{-13}$ of the entire decays (see the grey marked region of **b)**). Another downside are background counts in the spectra, making the zero crossing invisible [6].

In order to reach such a high precision in terms of mass measurements, it takes a highly technical setup (see Fig. 2.2). Therefore, a high luminously Windowless Gaseous Tritium Source (WGTS) is placed in the Source Section guiding up to 10^{11} tritium β-electrons per second into the Transport Section. By differential and cryogenic pumping the tritium flow rate then will be reduced by more than 12 orders of magnitude, lowering the background rate to less than $0.001\,\mathrm{cps}$ [8]. Subsequently the β-electrons reach the Spectrometer Section, where the Pre-Spectrometer and the Main Spectrometer analyse the kinetic energy of the β-electrons, using different retarding voltages. This MAC-E filter method, based on precedent experiments in Mainz and Troitsk, is able to record the integrated energy spectra of the tritium beta-decay with a design value for the energy resolution $\Delta E = 0.93\,\mathrm{eV}$ (for further information see Section 2.1.1) [8]. Beta-electrons passing the MAC-E filter will then be counted by the Focal Plane Detector (FPD). The FPD features high count rates ($< 1\,\mathrm{Mcps}$) but an energy resolution lower than $\mathrm{m}_{\bar{\nu}_e}$. Additionally for calibration and monitoring purposes, the KATRIN experiment encompasses a mono-energetic electron source (Egun) placed in the Rear Section [8].
Since the energy resolution of the FPD lacks to record energy spectra with a sensitivity in the sub-eV range, the MAC-E filter is part of the KATRIN experiment, enabling such precise measurements.

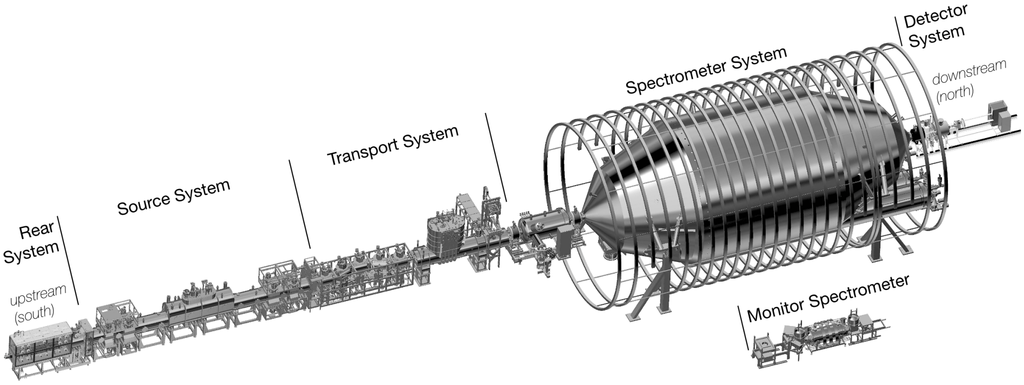

Figure 2.2.: Illustration of the 70 m long KATRIN setup located in Karlsruhe at the Karlsruhr Institut für Technologie (KIT) providing the highest sensitivity in direct neutrino mass measurements, by analysing the energy spectra of the the tritium beta-decay with help of the MAC-E filter [8].

2.1.1 MAC-E filter concept

The electron is born in the WGTS in a high magnetic field and is moving on cyclotron tracks (for the exact trajectory calculation $\vec{r}(t)$ see Eq. (4.8) of Chapter 4). Hence the kinetic electron energy is split in a longitudinal component $E_{\parallel}$, parallel to the B-field direction, and a transverse component $E_{\perp}$, perpendicular to it. The kinetic electron energy E_{kin} can then be written as following, with θ denoting the pitch angle between the magnetic field lines $\vec{B}$ and the positional vector of the electron $\vec{r}(t)$:

$$E_{\text{kin}} = E_{\parallel} + E_{\perp} = E_{\text{kin}} \cdot \cos^2(\theta) + E_{\text{kin}} \cdot \sin^2(\theta) \tag{2.5}$$

The MAC-E filter works with electrodes creating a retarding potential U_{ret} in the Analysing Plane (AP), which is located between entry and exit of the spectrometer vessel and orientated perpendicular to the magnetic field lines $\vec{B}$ in the vessel. For longitudinal electron energies $E_{\parallel}$ below the retarding energy eU_{ret} the MAC-E filter blocks, while for energies above the retarding energy, the MAC-E filter let the electron pass.

In the Source Section β-electrons are generated isotropically with an angular density distribution of $\rho(\theta) = \sin(\theta)$ [2]. Therefore the electrons have to be collimated before getting analysed within the AP. This means to transfer the energy portion of the transverse component into longitudinal direction. This is what makes the MAC-E filter so sensitive and the degree of collimation thus defines the energy resolution ΔE of the MAC-E filter. For KATRIN the design value for the energy resolution ΔE is

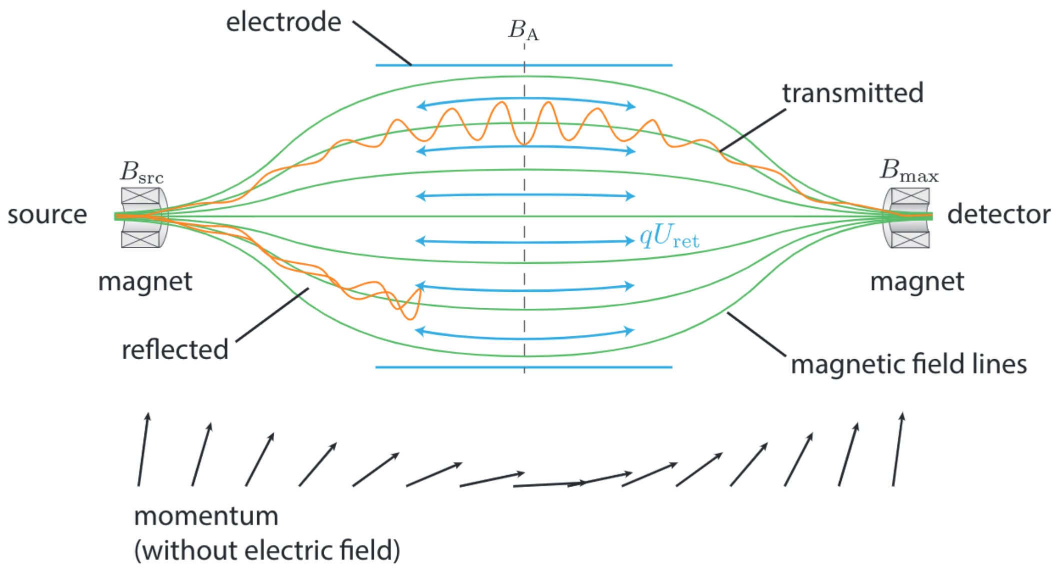

Figure 2.3.: Schematic view on the KATRIN spectrometer vessel, with green magnetic field lines, orange electron tracks starting at the source leading towards the detector and electrodes inducing an electric counter field (blue). While the electron labelled with 'reflected' is blocked by the MAC-E filter, the other one gets transmitted. The black arrows schematically indicate the momentum direction of the electron in absence of an electric field and hence illustrate the adiabatic collimation at the AP [3].

defined as following, with E_{max} denoting the maximal kinetic electron energy, $|\vec{B}_{\text{min}}|$ the minimal and $|\vec{B}_{\text{max}}|$ the maximal magnetic field strength [8]:

$$\Delta E = E_{\text{max}} \cdot \frac{|\vec{B}_{\text{min}}|}{|\vec{B}_{\text{max}}|} \tag{2.6}$$

$$\Delta E = 18.6\,\text{keV} \cdot \frac{0.3\,\text{mT}}{6\,\text{T}} = 0.93\,\text{eV} \tag{2.7}$$

The transfer of momentum can be achieved by the so-called magnetic adiabatic collimation of momentum under conditions of a radial symmetric and time invariant magnetic field. Adiabaticity also requires, that the magnetic field does not change to fast in space. Since these conditions are met in the KATRIN setup, the magnetic moment μ_{m} of the cyclotron motion is a constant resulting in the following expression [2]:

$$\mu_{\text{m}} = \frac{e}{2m_e}|\vec{l}| = \frac{E_\perp}{|\vec{B}|} \tag{2.8}$$

Using Eq. (2.8) the kinetic electron energy in transverse direction at the analysing plane $E_{\perp,\text{A}}$, can be calculated for an electron starting with the energy E_{kin} and the pitch angle θ in the Source Section at a magnetic field strength $|\vec{B}_{\text{src}}|$ and a defined magnetic field strength $|\vec{B}_{\text{A}}|$ at the AP:

$$E_{\perp,A} = E_{\text{kin}} \cdot \sin^2(\theta) \frac{|\vec{B}_{\text{A}}|}{|\vec{B}_{\text{src}}|} \tag{2.9}$$

The initial magnetic field strength $|\vec{B}_{\text{src}}|$ has to be above $|\vec{B}_{\text{A}}|$ in the AP to achieve electron collimation. From Eq. (2.5) the longitudinal energy $E_{||}$ can be derived.

$$E_{||} = E_{\text{kin}} - E_{\perp,A} \tag{2.10}$$

For $E_{||} > eU_{\text{ret}}$ the filter lets the electron pass. The transmission probability consequentially yields one. In all other cases the transmission probability is zero.

A transmission function has to take into account the finite energy resolution ΔE, resulting from a magnetic field strength $|\vec{B}_{\text{A}}|$ above zero, which makes it impossible (according to Eq. (2.9)) to transfer the whole transverse energy into longitudinal direction. Additionally, it should consider a maximum pitch angle θ_{max} at the source, for which electrons are transmitted. This maximum pitch angle originates in the magnetic mirror effect. It appears, while electrons travel along an increasing magnetic field, resulting in adiabatic decollimation. This is the case, if we consider the whole KATRIN spectrometer, where the magnetic field at the vessel entrance $|\vec{B}_{\text{src}}|$ is below the one of the vessel exit $|\vec{B}_{\text{max}}|$. The transverse energies of the electrons effectively rise:

$$E_{\perp,\text{max}} = E_{\text{kin}} \cdot \sin^2(\theta) \frac{|\vec{B}_{\text{max}}|}{|\vec{B}_{\text{src}}|} \tag{2.11}$$

For transverse energies above the initial kinetic energy ($E_{\perp,\text{max}} > E_{\text{kin}}$) the electron reverses its direction and the electron is effectively reflected. For θ_{max} meeting the reflection condition ($E_{\perp\text{max}} = E_{\text{kin}}$) Eq. (2.11) gives [3]

$$E_{\text{kin}} = E_{\text{kin}} \cdot \sin^2(\theta_{\text{max}}) \frac{|\vec{B}_{\text{max}}|}{|\vec{B}_{\text{src}}|} \tag{2.12}$$

$$\theta_{\text{max}} = \arcsin\left(\sqrt{\frac{|\vec{B}_{\text{src}}|}{|\vec{B}_{\text{max}}|}}\right). \tag{2.13}$$

KATRIN design values for $|\vec{B}_{\text{src}}| = 3.6\,\text{T}$ and $|\vec{B}_{\text{max}}| = 6.0\,\text{T}$ derive the maximal starting angles for electrons [8]

$$\theta_{\text{max}} = 50.77°. \tag{2.14}$$

The transmission function $T(E_{\text{kin}}, eU_{\text{ret}})$ for an electron with the starting energy E_{kin} then can be indicated as in Eq. (2.15) [2]. It does not take into account relativistic corrections.

$$T(E_{\text{kin}}, eU_{\text{ret}}) = \begin{cases} 0 & \text{if } E_{\text{kin}} - eU_{\text{ret}} < 0 \\ \frac{1-\sqrt{1-\frac{E_{\text{kin}}-eU_{\text{ret}}}{E_{\text{kin}}}\cdot\frac{|\vec{B}_{\text{src}}|}{|\vec{B}_{\text{A}}|}}}{1-\sqrt{1-\frac{|\vec{B}_{\text{src}}|}{|\vec{B}_{\text{max}}|}}} & \text{if } 0 < E_{\text{kin}} - eU_{\text{ret}} < \Delta E \\ 1 & \text{if } \Delta E < E_{\text{kin}} - eU_{\text{ret}} \end{cases} \tag{2.15}$$

Even though the energy resolution ΔE denotes the width of the transmission function, it does not limit the resolution of structures in the spectra. The knowledge of the transmission function, fully characterised by Egun measurements, helps to achieve even higher resolutions [8].

Due to scattering events while propagating through the source, the β-electrons are subject to energy loss before getting analysed by the MAC-E filter. The convolution of this energy loss function with the transmission function $T(E_{\text{kin}}, eU_{\text{ret}})$ from Eq. (2.15) then yields the response function $R(E_{\text{kin}}, eU_{\text{ret}})$. Subsequently, the signal rate at the detector $\dot{N}_s$ is a function of the retarding energy eU_{ret}, the endpoint energy E_0, the squared neutrino mass $m^2_{\bar{v}_e}$, the background count rate $\dot{N}_b$ and the number of tritium molecules (T_2) N_{tot} in the source. [2]:

$$\dot{N}_s\left(eU_{\text{ret}}, E_0, m^2_{\bar{v}_e}, \dot{N}_b\right) = \dot{N}_b + N_{\text{tot}} \cdot \int_0^{E_0} \frac{\mathrm{d}N}{\mathrm{d}E_{\text{kin}}}\left(E_{\text{kin}}, E_0, m^2_{\bar{v}_e}\right) \cdot R(E_{\text{kin}}, eU_{\text{ret}}) dE_{\text{kin}} \tag{2.16}$$

Given Eq. (2.16) the β-spectra $\frac{\mathrm{d}N}{\mathrm{d}E_{\text{kin}}}$ from Eq. (2.3) contributes within the integral to the measured count rate at the FPD.

2.1.2 Background induced by Rydberg atoms

The count rate measured in the KATRIN experiment is affected by various types of background. Among these, electrons from the spectrometer walls, radon decay induces electrons, magnetically trapped electrons and ionized Rydberg atoms can be mentioned. This four types account for the actual background count rate of about $293\,\text{mc/s}$, which is more than a magnitude higher than the envisaged background count rate of $10\,\text{mc/s}$. Three of the four types were successfully minimised, leaving the ionized Rydberg atoms as the main contributor for the KATRIN background [8] [9].

This so-called Rydberg background results from the $^{222}_{86}\text{Rn}$ contamination of the Main Spectrometer. During construction the Main Spectrometer was exposed to ambient air, which naturally contains $^{222}_{86}\text{Rn}$. One of its daughter nucleis then was accelerated throughout the ${}^{222}_{86}\mathrm{Rn}$ decay and was therefore implanted into the vessel wall. The decay chain of ${}^{222}_{86}\mathrm{Rn}$ leads to the lead isotope ${}^{210}_{82}\mathrm{Pb}$ with a half-life time of $22.3\,\mathrm{yr}$. Consequentially the displayed decay chain ${}^{210}_{82}\mathrm{Pb} \rightarrow {}^{206}_{82}\mathrm{Pb}$ is at the moment the dominant process on the Main Spectrometer walls [1]:

$$ {}^{210}_{82}\mathrm{Pb} \rightarrow {}^{210}_{83}\mathrm{Bi} + e^{-} + \bar{\nu}_e \tag{2.17}$$

$$ {}^{210}_{83}\mathrm{Bi} \rightarrow {}^{210}_{84}\mathrm{Po} + e^{-} + \bar{\nu}_e \tag{2.18}$$

$$ {}^{210}_{84}\mathrm{Po} \rightarrow {}^{206}_{82}\mathrm{Pb} + {}^{4}_{2}\mathrm{He} \tag{2.19}$$

Due to the high recoil energy released in the α-decay from Eq. (2.19), an off-sputtering of mainly hydrogen atoms from the surface wall may occur. Additionally, the released energy can induce highly excited states of the hydrogen atom and thus generate Rydberg atoms. These highly excited states feature low ionisation energies of a few meV. While charged Rydberg atoms are prohibited from entering the Main Spectrometer by the Inner Electrode System, neutral Rydberg atoms are able to enter the flux tube of the Main Spectrometer unhindered and overcome all magnetic and electrical barriers. Secondary electrons generated in the ionisation process inside the flux tube can then be accelerated onto the FPD and get counted as β-electrons and thus produce the aforementioned background.

Besides field ionisation and ionisation induced by residual gas collisions, the ionisation through black body radiation is considered to be the main ionisation mechanism for these Rydberg atoms [8]. At room temperature $T = 293\,\mathrm{K}$ the typical initial electron energy E_{Ryd} is around

$$E_{\text{Ryd}} \approx kT = 25\,\mathrm{meV} \tag{2.20}$$

resulting from the energy spectra of a black body radiation [9]. Since the electrons are produced at low energies in the meV range, they are not able to overcome the retarding energy of the MAC-E filter in the keV range. Hence the volume behind the AP determines the amount of Rydberg background contributing to the overall KATRIN background [8].

One background reduction method is to reduce the volume behind the AP. This was performed in 2020 for regular tritium campaign by introducing the Shifted Analysing Plane (SAP) (see Fig. 2.4), which enhances the signal to background ratio by a factor two [10].

Furthermore a spectrometer bake-out, performed during maintenance work in 2020 managed to reduce the amount of impurities on the spectrometer surface, so that less Rydberg atoms are sputted off [10].

A UV irradiation system was additionally installed, in order to improve the surface conditions of the Main Spectrometer hoping to reach a significant impact on the Rydberg background. But until now, there was no of such expected background

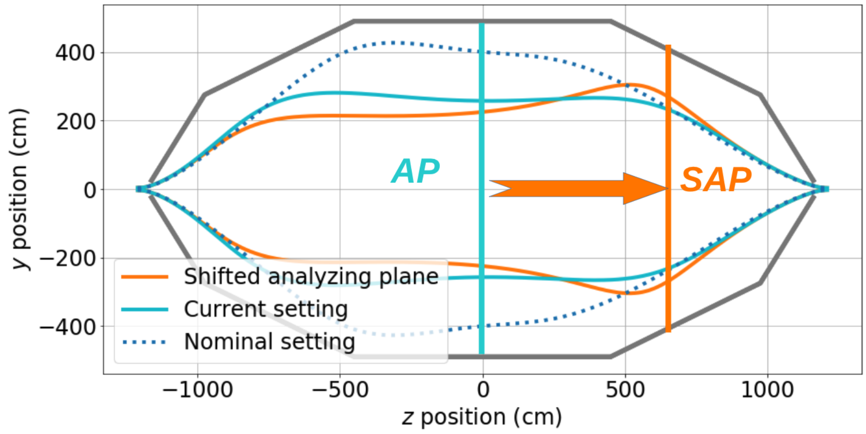

Figure 2.4.: Schematic view on the flux tube in the Main Spectrometer, in AP and SAP setting. The SAP reduces the volume behind the AP and thus suppress the Rydberg background [10].

improvement [8].
However until now this Rydberg background is still a hypothetical explanation for the elevated KATRIN background. Even though tests with installed α-sources showed similar dependencies as the Rydberg background and therefore provided a confirmation of the Rydberg hypothesis [4].
In case this Rydberg hypothesis proves to be correct, the active Transverse Energy Filter (aTEF) is a promising candidate capable of reducing the Rydberg background significantly.

2.1.3 active Transverse Energy Filter (aTEF)

The aTEF is an idea based on the Transverse Energy Filter (TEF) concept, initiated by R. G. H. Robertson in 2019. The goal of both concepts is to separate β-electrons from Rydberg background induced electrons by means of a filter.
Premise is the difference in transverse electron energies at the AP between background and beta electrons. Assuming an isotropic angular distribution of background electrons at its generation, leads to maximal transverse energies at the AP $E_{\perp,\mathrm{Ryd,A}}$ in the order of the ionisation energy (see Eq. (2.20))[9].

$$E_{\perp,\mathrm{Ryd,A}} \approx 25\,\mathrm{meV} \tag{2.21}$$

In contrast to that, the maximal transverse energy of β-electrons at the AP $E_{\perp,\mathrm{sig,A,dsg}}$ differs by more than an order of magnitude for the Design-setting [8].

$$E_{\perp,\mathrm{sig,A,dsg}} = 930\,\mathrm{meV} \tag{2.22}$$

For the actual standard setting the difference is even bigger, with $E_{\perp,\text{sig,A,std}}$ denoting the associated transverse energy at the AP [8].

$$E_{\perp,\text{sig,A,std}} = 2.77\,\text{eV} \tag{2.23}$$

The filter could be placed between the pinch magnet ($|\vec{B}_{\text{max}}|$) and the FPD at a magnetic field strength of approximately $0.5\,\text{T}$ (alternative filter positions, such as directly in front of the detector, are also being considered). Taking into account the considerably lower magnetic field strength at the AP of $|\vec{B}_{\text{AP}}| = 3 \cdot 10^{-4}\text{T}$, both the signal and background electrons get adiabatically decollimated on the way towards the filter (see Section 2.1.1). The resulting transverse energy distributions differ in energy position and shape at the filter and correspond via Eq. (2.5) to a different angular distribution $\rho_{\text{filter}}(\theta)$ at the filter position (see Fig. 2.5 **(b)**).

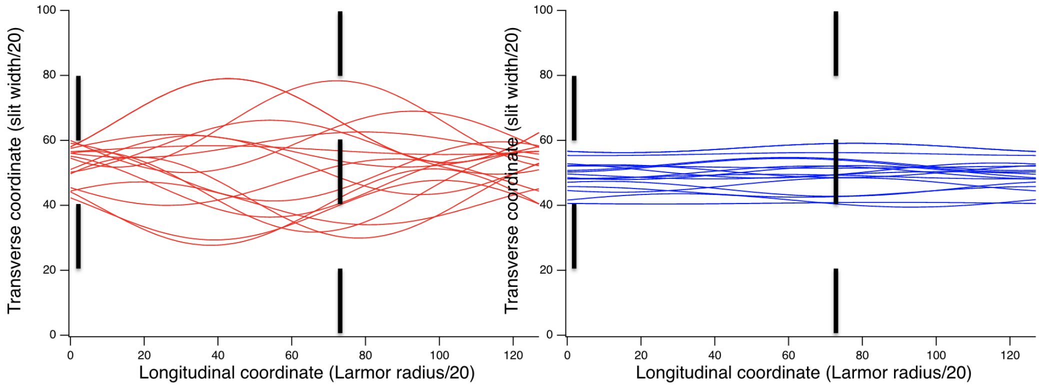

(a) TEF principle

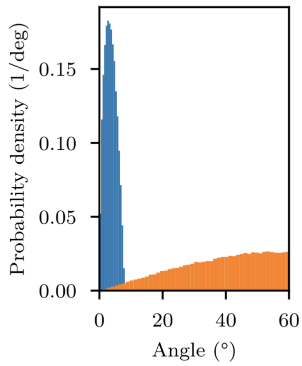

(b) angular distribution $\rho_{\text{filter}}(\theta)$

Figure 2.5.: In **(a)** the TEF principle is illustrated, simulating signal electrons (red) with the respective angular distribution form **(b)** (orange). Rydberg background electrons (blue) with the respective angular distribution (blue) are also simulated. The different probability to hit the wire grids makes a filtering of the background electrons possible. The angular distribution of **(b)** is based on false assumptions on the maximal kinetic energy of Rydberg induced electrons. Additionally the simulations were conducted with a wrong magnetic field setting. But it serves for illustration purposes. The plots were taken from [9] and [11].

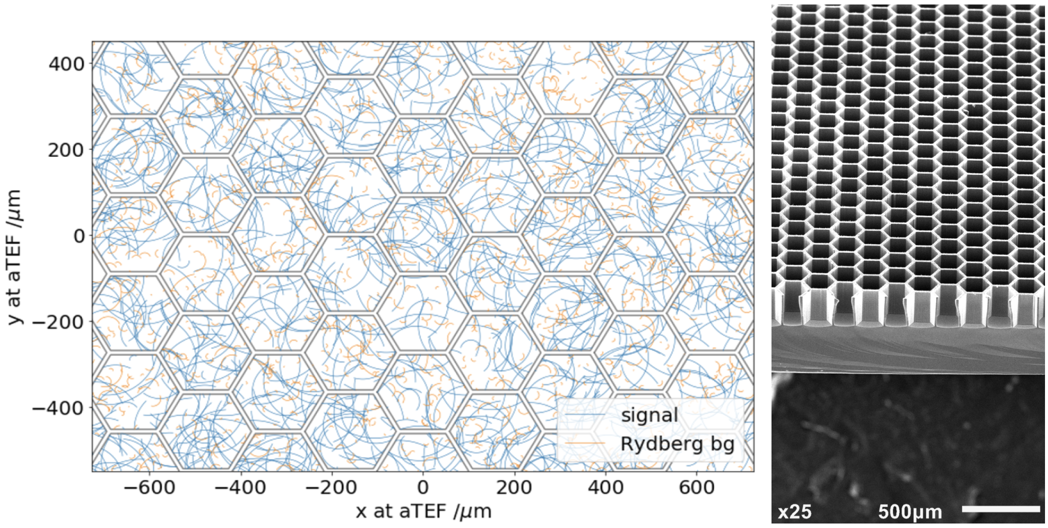

(a) simulation on the planned aTEF

(b) preliminary etching results

Figure 2.6.: In **(a)** a Monte Carlo simulation on the planned aTEF is displayed (C. Weinheimer, personal communication, July 13, 2021). The differing electron tracks (signal electrons in blue and Rydberg background induced electrons in orange) make it more probable for signal electrons to hit the hexagonal aTEF structures. In **(b)** a scanning electron microscope picture of the preliminary etching results for the aTEF manufacturing process is shown (K. Gauda, personal communication, July 13, 2021).

The TEF consists of two shifted wire grids spaced a wire diameter apart [9]. Hence, just β-electrons will be transmitted, while background electrons with gyroradii r_g (corresponds to the sine of θ via $r_g = \frac{v_\perp}{\omega_c} = \sin(\theta) \cdot \frac{v_0}{\omega_c}$ with ω_c being the larmor frequency of the cyclotron motion. For a more detailed description see the calculations of Chapter 4) smaller than these of the β-electrons are more likely to hit the wire grids of Fig. 2.5.
But since the TEF is subject to a veritable signal loss of the factor 3.6 with simultaneous background mitigation of the factor 20, there is no improvement in neutrino mass sensitivity [12].

The aTEF shall improve the the ratio of signal loss to background suppression. Instead of wire grids, the aTEF has a capillary filter design. Therefore a silicon wafer with a depth in the order of $500\,\mu\mathrm{m}$ will be etched through, resulting in hexagon structured holes with a side length in the $100\mu\mathrm{m}$ scale like in Fig. 2.6. Preliminary etching results are depicted in Fig. 2.6. Featuring the edged wafer with an activation layer, will thus enable the active filter to generate secondary electrons, in case an electrons hits the activation layer inside the aTEF hole. The separation between β and background electrons then happens, due to differing activation-layer-hit-probabilities for different angular distributions (see Fig. 2.5).
This thesis encompasses crucial conceptual tests in the working principle of such an aTEF and therefore aims to show that electrons hitting the activation layer produce

secondaries, which then can be distinguished from single electrons. For this purpose we used a Microchannel Plate (MCP) instead of the actual aTEF, which did not exist at the time of experiment. As described in Section 3.2.1 the MCP works analogously to the aTEF and differs only in dimensions and material, where the latter aims to omit the intrinsic lead glass background of an MCP. While the production of aTEF prototypes requires time for research and development, industry-manufactured MCPs are quickly available for the tests and proof-of-concept measurements.

3 aTEF test setup in Münster

To test the aTEF working principle it takes an Ultra High Vacuum (UHV) setup which can imitate the conditions of the filter region (for location proposals see Section 2.1.3) at the KATRIN experiment. The test Setup (in the following called aTEF setup), constructed in Münster, fulfills these requirements at a UHV of $10^{-7}\mathrm{mbar}$. It consists of an Egun generating mono-energetic electrons at a defined Egun tilt angle α_p. Water and air cooled coils produce an approximately radial symmetric magnetic field, able to guide the electrons trough the MCP filter at the center towards the MCP detector at the end of the setup (see Fig. 3.1). This setup permits a nearly adiabatic transport of the electrons [13].
The individual components, consisting of the electron source (Egun), the MCP filter and the MCP detector, are described in more detail within the following sections.

3.1 Mono-energetic electron source (Egun)

The Egun (see Fig. 3.2 for the schematic drawing) is an integral part of the aTEF setup. It generates electrons at a defined kinetic electron energy E_e and a modifiable Egun tilt angle α_p.
By the photoelectric effect, the generation of single electrons is caused. An LED is providing UV light with a wavelength of $\lambda = 265\,\mathrm{nm}$ and a photo energy of $h\nu = hc/\lambda = 4.7\,\mathrm{eV}$. This photo energy is sufficient to exceed the work function Φ for an electron of a thin gold or silver coated photocathode ($\Phi < 5\,\mathrm{eV}$ dependent on surface roughness, impurities and the Schottky effect [14]). The electron then has a kinetic energy $E_e = hc/\lambda - \Phi$ in the order of $1\,\mathrm{eV}$.
The photocathode is integrated in the back plate of the Egun, which is set to a negative electric potential U_back. Since the front plate is connected to a voltage divider $U_\mathrm{front} = U_\mathrm{back} + U_\mathrm{acc} = \frac{3}{4}U_\mathrm{back}$, generating a potential gradient of U_acc, the electron gets electrostatically accelerated towards the front plate. Thus the electron gets collimated towards the surface normal of both plates with an angular spread [14].
In addition to the electric field, there is a constant magnetic field $\vec{B}(z) = \vec{B}$ with

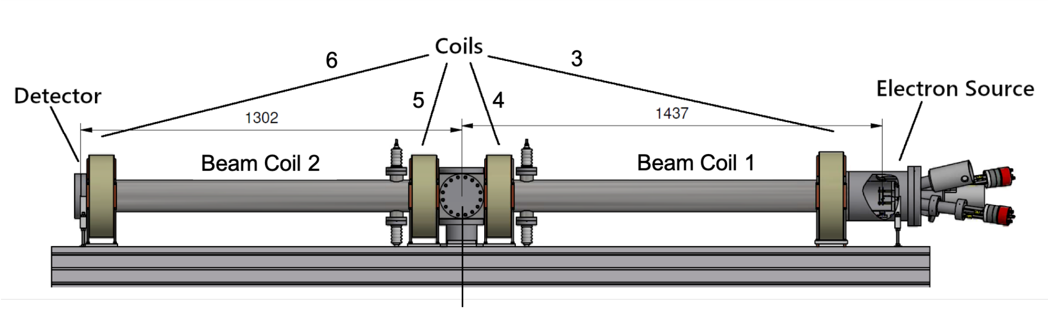

Figure 3.1.: CAD drawing, made by H.-W. Ortjohann, of the aTEF test setup in Münster. It composes a vacuum chamber system, with a mono-energetic and angular selective electron source (Egun) at the one end, the MCP filter in the center and the MCP detector at the other end. The setup features 4 water cooled coils (coils 3-6) and two air cooled coils (beam coil 1 and 2). The whole setup is approximately $3\,\mathrm{m}$ long [13].

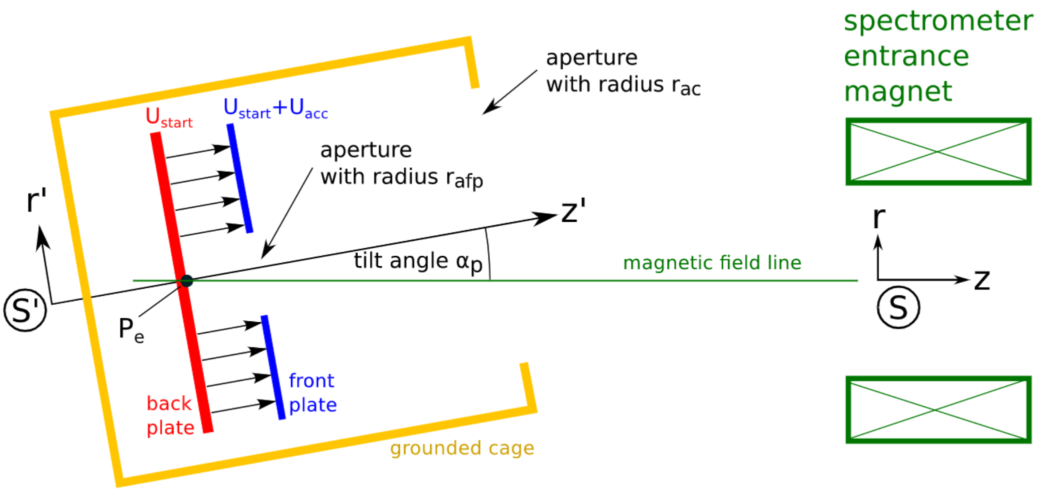

Figure 3.2.: Schematic view on the Egun, that is able to generate electrons on a cyclotron track. Therefore electrons are released at P_e through the photoelectric effect and get accelerated with the positive potential gradient U_{acc} towards the front plate. The Egun tilt angle α_{p} determines the transverse energies of the electrons, when leaving the acceleration area. The grounded cage shields the Egun from outside influences and ensures a homogeneous electric field [14].

an angle α_p between the field lines and the surface normal of front and back plate. Consequentially the electron motion is affected by the Lorentz force [14]:

$$\vec{F_L} = e(\vec{E} + \vec{v} \times \vec{B}) \tag{3.1}$$

Generated at low kinetic energies E_e (corresponds to small velocities v) in a strong electric field $\vec{E}$ the electron is accelerated non-adiabatically up to initial kinetic energies of $E_e = eU_\text{back}$. In this acceleration area, firstly the electric field $\vec{E}$ is dominant until the magnetic field takes over while v rises steadily. That enables an adiabatic transport along the magnetic field lines.
After leaving the acceleration range, the electron performs a cyclotron motion, which depends on the transverse electron energy:

$$E_{e,\perp} = E_e \cdot \sin^2(\theta) \tag{3.2}$$

As long as the transport of the electron happens adiabatically the pitch angle θ determines the gyroradius r_g (see calculations of Chapter 4):

$$r_g \propto \sin(\theta) \tag{3.3}$$

Such an adiabatic transport can be assumed to be approximately given for the aTEF setup [13].
Moreover the pitch angle θ at a magnetic field strength B_θ is directly connected to the Egun tilt angle α_p from Fig. 3.2. The non-linear relation is described by Eq. (3.4), where k denotes a scaling factor resulting from the non-adiabatic transport and B_start the magnetic field strength at the Egun [14].

$$\theta \approx \arcsin\left(\alpha_\text{p} \cdot k \cdot \sqrt{\frac{B_\theta}{B_\text{start}}}\right) \tag{3.4}$$

For the case $B_\theta = B_\text{start}$ the produced pitch angle θ is smaller than this of the Egun plate α_p.
To modify the Egun plate angle α_p and analogously θ, the plate system is mounted inside a ground cage on top of a gimble. This gimble is controlled by air pressure driven step motors able to work under UHV conditions [14]. With help of a LabView program the desired polar and azimuth angle can be set [2].

During measurements the voltage at the Egun back plate was chosen to stay constant at $U_\text{back} = -1\,\text{kV}$ resulting in an initial kinetic electron energy $E_e \approx 1\,\text{keV}$. Only the Egun plate angle α_p was modified, intending to vary the gyroradius of the electron cyclotron motion.
Throughout Egun operation, the LED was pulsed with the Tektronix AFG 3102 function generator, generating $8\,\text{V}$ rectangle pulses of $100\,\text{ns}$ width with a $10\,\text{kHz}$

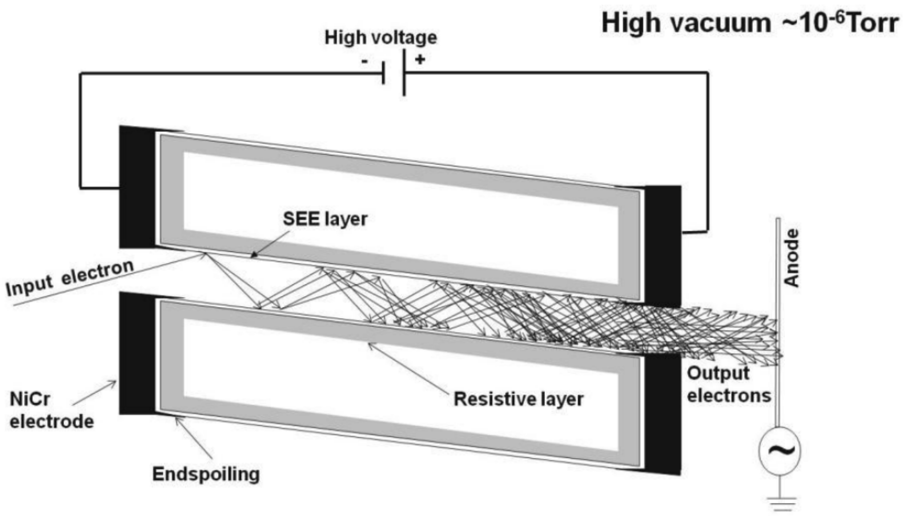

Figure 3.3.: Schematic drawing of a single MCP channel with a bias angle, showing secondary electron yield induced by an electron hitting the MCP channel wall [15].

frequency. Not at every pulse an electrons will be released, so that the electron rate is lower than the pulse frequency.

3.2 Microchannel Plate (MCP)

MCPs are low threshold signal detectors, made of lead glass, able to detect single electrons or photons in a high vacuum environment. For our purpose the MCP is on the one hand used as a filter and on the other hand as a detector (see Section 3.2.1 and Section 3.2.2).

The MCP is a two dimensional array of multiple electron multiplier tubes with typical diameters in the µm range (see Fig. 3.3 for one tube). Equipped with an SEE layer on the channel wall, the MCP yields secondary electrons inside the tube, in case an electron has hit the wall and "sees" a positive voltage gradient. This voltage gradient is generated by applying high voltages of around $1\,\mathrm{kV}$ between the front and the back electrode of the MCP. The resulting uniform electrostatic field inside the channel accelerates the secondary electrons towards the MCP back electrode, generating further channel wall hits [15]. Subsequently the MCP outputs a cascade of $10^3 - 10^5$ secondary electrons (see Fig. 3.3). The SEE coefficient, as well as the angle and location of incidence inside the MCP channel, defines the respective secondary electron yield [16]. To prevent ion feedback, which can destroy the MCP, the MCP channels usually have a bias angle of a few degrees. Additionally MCPs often operate in stack configuration. While the chevron stack denotes two MCPs laid on top of each other with shifted channel direction, the Z-configuration includes 3 MCPs.

To ensure the electron recharge after release, the MCP comes with intrinsic resistances of $(10 - 500)\mathrm{M\Omega}$. That also prevent thermal overheating of the MCP induced by large currents [16].
Every MCP is naturally subject to a dark count rate, which consists of its intrinsic lead glass background and radioactive decays in ambient air. This dark count rate can easily be made accessible via count rate measurements with the Egun switched off.

3.2.1 MCP filter

The MCP used as filter is a single MCP manufactured by Roentdek. It features a channel diameter of $10\,\mathrm{\mu m}$, a channel depth of $400\,\mathrm{\mu m}$ and a bias angle $\alpha = 12°$. The active area counts $25\,\mathrm{mm}$ diameter and has an open area ratio OAR of $60\,\%$ resulting in channel distances of $12.5\,\mathrm{\mu m}$ (H. W. Ortjohann, personal communication, January 15, 2021).
In order to place the MCP inside the beam tube, it was fixed with two copper rings in a synthetic MCP holding device (hereinafter referred to as MCP holder). These copper rings provide the differential voltage, to operate the MCP in active mode, capable of Secondary Electron Emission (SEE). The MCP holder is again attached to a linear feed through with a screw, allowing to modify the tilt angle of the MCP plane. The linear feed through and two high voltage connectors (type description: Coaxial SHV 20 kV by Hositrad) are mounted onto a CF100 flange. A Computer-Aided Design (CAD) drawing of this MCP setup is shown in Fig. 3.4.
The CF100 flange is attached to the cube flange between the two centered coils 4 and 5 of the aTEF setup. At this location a nearly homogeneous magnetic field environment is given.
Due to the difficult installation of the MCP filter inside the aTEF setup, resistance measurements after its insertion have yielded $R \approx 225\,\mathrm{M\Omega}$, indicating the MCP filter is still working as secondary electron emitter.

In case the MCP is operated in active mode two high voltage connectors and a voltage divider permit to set the front electrode of the MCP on a more negative voltage as the back electrode (differential voltage $U_{\text{diff}} = -750\,\mathrm{V}$), allowing SEE. At the same time the two high voltage connectors permit to set both, MCP front and back, on the same more negative voltage (reference voltage $U_{\text{ref}} = -50\,\mathrm{V}$), to generate a small electric field between filter and detector that accelerates secondary electrons towards the latter.

$$U_{\text{MCP, back}} = U_{\text{ref}}$$
$$U_{\text{MCP, front}} = U_{\text{ref}} + U_{\text{diff}}$$

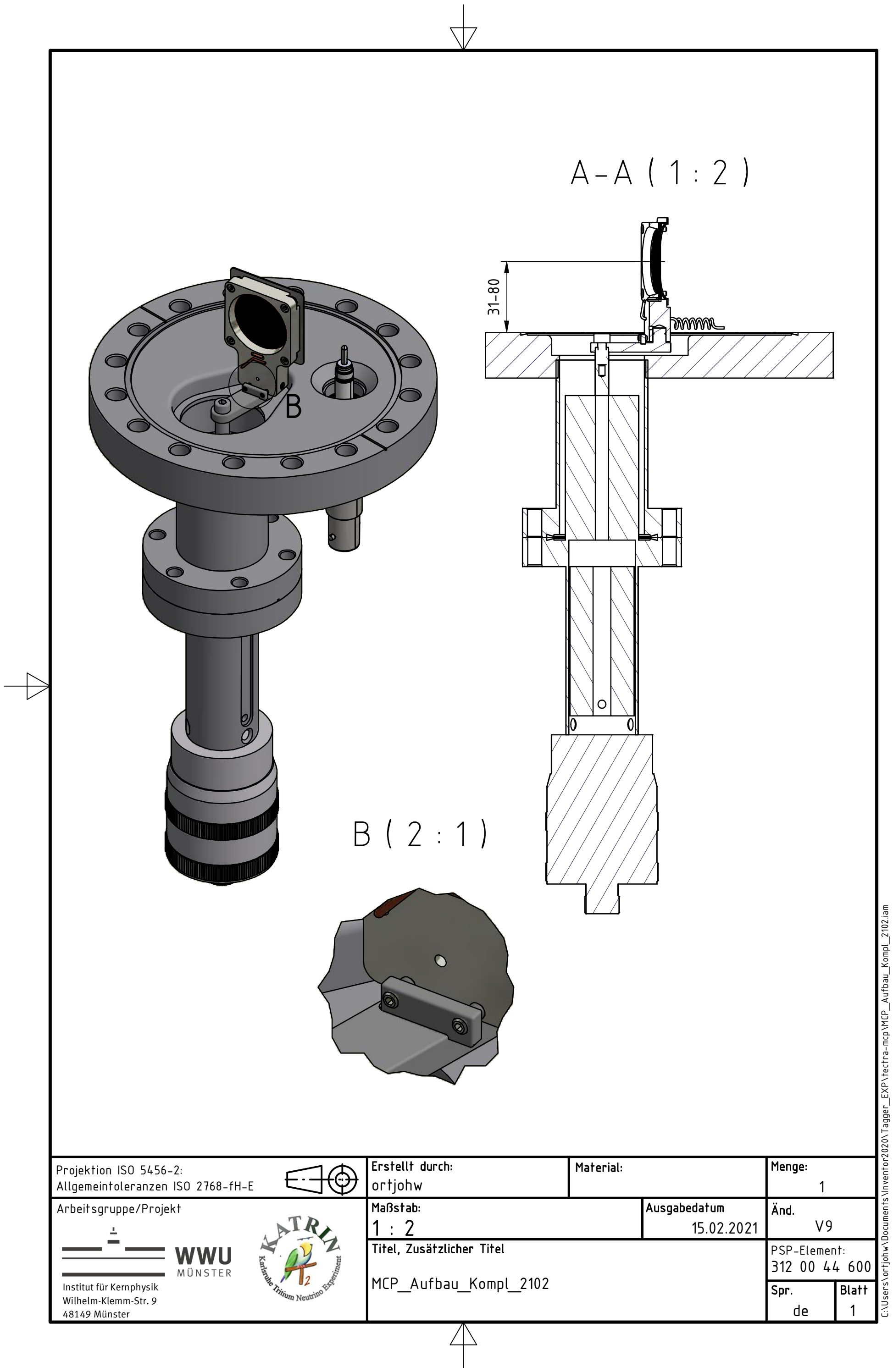

Figure 3.4.: CAD drawing shows the CF100 flange, with the two high voltage connectors and a linear feed through. The MCP is attached to the MCP holder, which is then mounted on top of the linear feed through (H.-W. Ortjohann, personal communication, March 13, 2021).

The negative potential at the MCP front of a total of $-750\,\mathrm{V}$ induces an electric counter field and therefore reduces the kinetic electron energy. But since the measurements were performed at initial longitudinal electron energies $E_{\|} = E_e \cdot \cos^2(\theta) \approx E_e = 1\,\mathrm{keV}$ (approximation applies for pitch angles θ in the order of degrees), the retarding potential does not fully block the electrons.
As high voltage source we used FuG HNC 35M-5000 for U_{diff} and iSEG NHQ 224M for U_{ref}.

3.2.2 MCP detector

In order to detect single electrons, as well as an avalanche of secondary electrons, two MCPs in chevron stack, manufactured by tectra Gmbh, was placed on a CF100 flange at the end of the aTEF setup. The used MCP detector has a channel diameter of $10\,\mu\mathrm{m}$, a channel depth of $400\,\mu\mathrm{m}$ and a bias angle of $6°$. The active area was indicated as $44\,\mathrm{mm}$ in diameter, featured with a $60\,\%$ OAR [17].
Precursor measurements of P. Oelpmann required the channel direction of the MCP filter to point in beam tube direction [18]. Therefore, the flange plane is inclined by the bias angle of $6°$. Uncertainties in the exact bias angle of the MCP detector causes the MCP detector phase effect, discussed in Chapter 6. This phase effect would be significantly larger, in case the MCP detector would not have been mounted on a slanted flange.
Since the MCP configuration operates as detector, a positive differential voltage between front and back of $1853\,\mathrm{V}$ was applied, enabling the detection of single electrons.

3.3 Operation of the aTEF test setup

For the purpose of this measurement, we want to only count the incoming electrons. Therefore the MCP signal (a typical signal is shown in Fig. 3.5) passes through a series of NIM modules.
After getting amplified through the 474 Timing Filter Amplifier (TFA) by ORTEC (coarse gain at 20 and fine gain out; integration and differential time are both $20\,\mathrm{ns}$ in Chapter 6, but vary throughout the measurements of Chapter 7), the amplified signal is discriminated in the Mod. N417 discriminator by CAEN at a threshold set to $100\,\mathrm{mV}$ producing rectangular pulses of a $100\,\mathrm{ns}$ width. In order to count both, single electrons and MCP-filter-multiplied electrons as one signal, one has to enlarge the evaluated rectangular pulse in time, circumvent the problem, that secondary electrons could have time distances of more than $100\mathrm{ns}$, which would result in multiple MCP detector signals. From Section 3.1 the UV-LED pulse rate of $10\,\mathrm{kHz}$ is known. Even though the Egun is not able to release an electron at

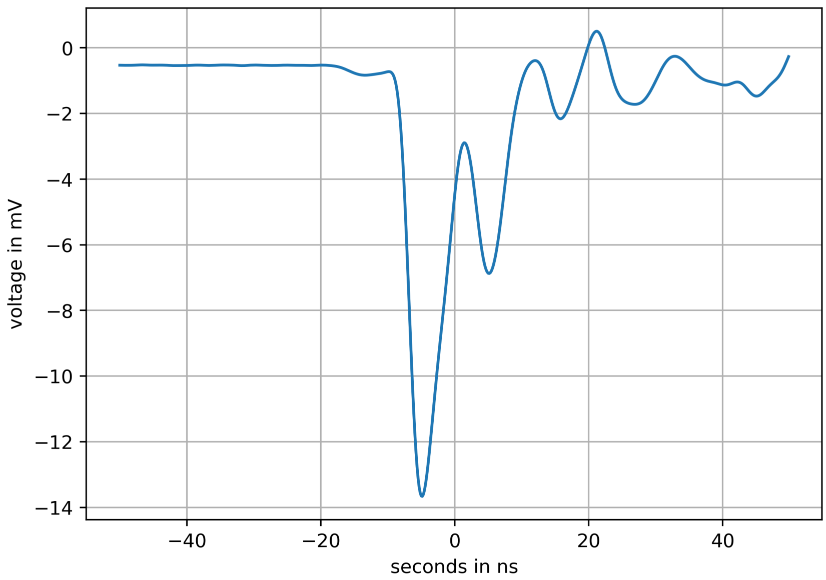

Figure 3.5.: Unamplified signal at the MCP detector output, induced by an electron-channel-wall-interaction.

every function generator event, it can be derived that the time distance of signal electrons is larger than $100\,\mu s$. With this knowledge the discriminated signal passes the G43 Gate Generator, manufactured by the university of Heidelberg, enlarging the rectangular signal onto $100\,\mu s$. An exemplary MCP detector signal for a single electron and for an avalanche of secondary electrons at every NIM component is displayed in Fig. 3.6.
Subsequently the enlarged rectangular signal of the signal type NIM has to be converted into a TTL signal able to be analysed by the NI-USB 6008 pulse counter by National Instruments. The pulse counter is then read out by the LabView program, developed by P. Oelpmann. The signal chain is shown again schematically in Fig. 3.7.

Optionally the current of beam coil 1 can automatically be swept in a defined interval with help of the aforementioned LabView program. Each set current can then be assigned a signal count rate. During all measurements, the other coils from Fig. 3.1 operate at currents displayed in Table 3.1.

Table 3.1.: Coil current configuration used for passive and active MCP filter measurements from Chapter 6 and Chapter 7. Uncertainties are due to reading inaccuracies of the power supply display.

	beam coil 1	beam coil 2	coil 3	coils 4 & 5 (parallel)	coil 6
Current in A	varies	11.20 ± 0.03	18.0 ± 0.3	10.0 ± 0.3	19.3 ± 0.3

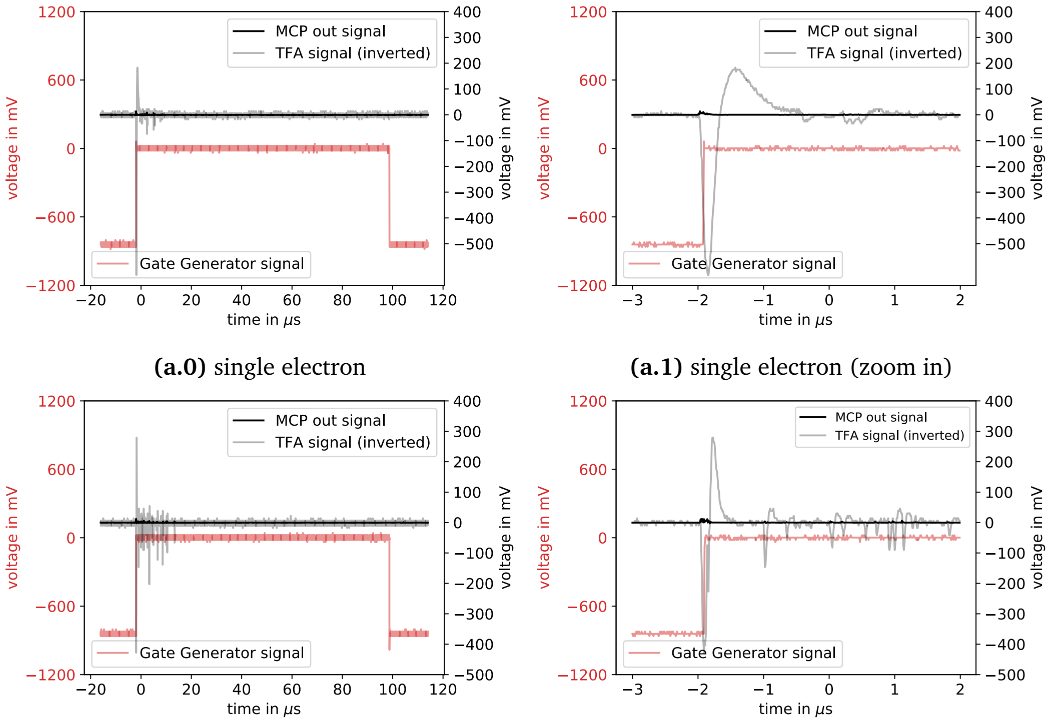

(a.0) single electron

(a.1) single electron (zoom in)

(b.0) avalanche of electrons

(b.1) avalanche of electrons (zoom in)

Figure 3.6.: Shape of the MCP out signal, the TFA-amplified MCP out signal and the pulse sensitive Gate Generator signal of $100\,\mu\mathrm{s}$ for a single signal electron (see **(a)**) and an avalanche of secondary electrons, generated by the MCP filter (see **(b)**).

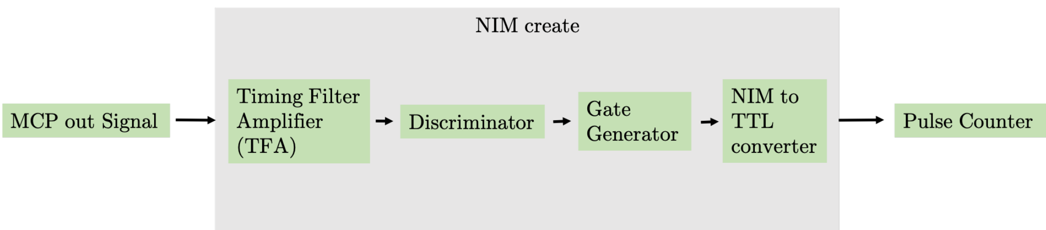

Figure 3.7.: Signal chain for the analysis of the incoming MCP detector signals at the aTEF test setup.

4 Monte Carlo simulation of passive MCP filter measurements

Filter properties of an MCP were already discovered in P. Oelpmanns work [18]. But before we designed and completed the aTEF setup as described in Chapter 3, it was to further investigate how the MCP shall behave in theory as filter. Therefore a simulation was needed, which rebuilds the geometry of the MCP. Plus, the simulation should be capable of producing a large amount of electrons at different pitch angles θ and thus imitate an angular selective and mono-energetic electron source (Egun). Apart from this, the simulation should be able to register these electrons, which hit the MCP wall. In total, this simulation should qualitatively predict certain results of the passive MCP filter measurements from Chapter 6. As basis we used a Python-3-based simulation, developed by C. Weinheimer and A. Fulst.

4.1 Simulation concept

This simulation and its further development includes the electron track calculation, which results from an emitted electron with a defined energy (here $E_{\text{kin}} = 1\,\text{keV}$ as in Chapter 6) and a defined pitch angle θ to the main magnetic field line. We used a B-field strength $|B| = 0.01\,\text{T}$ for the magnetic field at the Egun, which is in the order of the experimental value for the aTEF setup[1] [13]. This leads to a gyro motion, with the longitudinal component of the trajectory pointing towards magnetic field lines, while the transverse component rotates around it (see Fig. 4.1). The magnetic field lines represent the direction of the propagation of the electron's guiding center. For the MCP being in original position as in Fig. 4.3, the z-axis is parallel the main magnetic field lines. We make the following considerations to obtain an exact description of the electron movement.

[1]For later simulation result discussions, the exact value of $|B|$ at the Egun is not of importance, because the simulation only aims for a qualitative description of the MCP filter properties and does not take adiabatic collimation/decolliamtion of the electron into account anyway. Furthermore the exact relation between Egun tilt angle α_{p} and electron pitch angle θ is unknown, because of the lack of knowledge about the scaling factor k from Eq. (3.4).

The gamma factor of the electron, with the electron mass m_e and an initial energy of $E_0 = 1\,\mathrm{keV}$ is given by Eq. (4.1) [2].

$$\gamma = \frac{1}{\sqrt{1-\frac{v^2}{c^2}}} = 1 + \frac{E_{\text{kin}}}{m_e c^2} = 1.002 \approx 1 \tag{4.1}$$

Considering the low kinetic energy of the electron, compared to its rest mass $m_e c^2$, it is sufficient to calculate non-relativistic. The following expression of Eq. (4.2) for the kinetic energy then applies, so that the electron velocity v_0 can be derived:

$$E_0 = \frac{1}{2} m_e \cdot v_0^2 \tag{4.2}$$

$$v_0 = \sqrt{\frac{2E_0}{m_e}} \tag{4.3}$$

Splitting up the electron movement in a longitudinal $v_\parallel$ and a transverse $v_\perp$ component, taking into account the angle θ between $\vec{B}$ and $\vec{v}$, gives Eq. (4.4).

$$\vec{v} = \begin{pmatrix} v_\perp \\ v_\parallel \end{pmatrix} = \begin{pmatrix} v_0 \sin(\theta) \\ v_0 \cos(\theta) \end{pmatrix} \tag{4.4}$$

Considering the Lorentz force acting on the electron in a homogeneous and spatially constant magnetic field $\vec{B}$, we can describe the movement of an electron throughout the following equation of motion [19]:

$$m_e \cdot \dot{\vec{v}} = e \cdot \vec{v} \times \vec{B} \tag{4.5}$$

In case the magnetic field points in z-direction ($\vec{B} = B \cdot \vec{e}_z$) the periodical solution of the differential Eq. (4.5) yields the gyrofrequency ω_c.

$$\omega_c = \frac{e \cdot B}{m_e} \tag{4.6}$$

The trajectory of the electron $\vec{r}(t)$ is then described in Eq. (4.8) with the gyroradius r_g being proportional to the pitch angle θ:

$$r_g = \frac{v_\perp}{\omega_c} = \frac{v_0 \sin(\theta)}{\omega_c} \tag{4.7}$$

The electron trajectory of Eq. (4.8) is schematically illustrated in Fig. 4.1.

$$\vec{r}(t) = \begin{pmatrix} r_g \cos(\omega_c t) \\ r_g \sin(\omega_c t) \\ v_\parallel t \end{pmatrix} \tag{4.8}$$

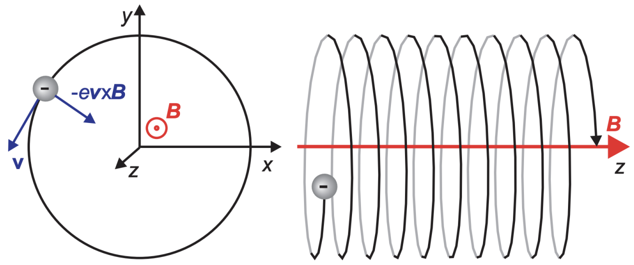

Figure 4.1.: Illustration of a cyclotron movement for an electron induced by a magnetic field pointing in z-direction [19].

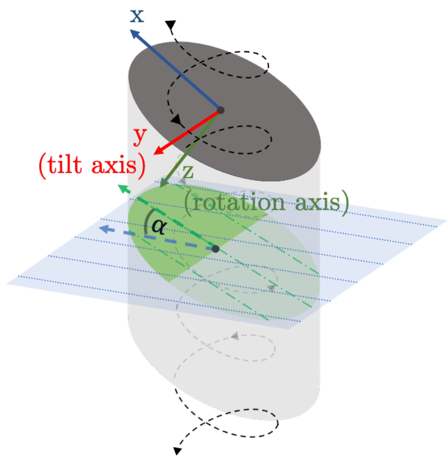

Figure 4.2.: Schematic sketch of an MCP channel, imagined as a diagonally cut tube. In this display the bias angle α is neutralised (tilt angle $= \alpha$; rotation angle $= 0°$). This means, that the magnetic field lines are parallel to the MCP channel direction. The resulting cyclotron motion of the electron, with a gyroradius smaller than this of the MCP channel, is shown in dashed lines.

Moving a distance $d = v_{\|}\Delta t$ in z-direction leads to a phase change in the circular electron movement of $\Delta\phi_{\text{gyro}} = \Delta t\omega_c = \frac{d\omega_c}{v_{\|}}$. That gives an electron trajectory $\vec{r}(d)$ with respect to d:

$$\vec{r}(d) = \begin{pmatrix} r_g \cos\left(\frac{d\omega_c}{v_{\|}}\right) \\ r_g \sin\left(\frac{d\omega_c}{v_{\|}}\right) \\ d \end{pmatrix} \tag{4.9}$$

In the Monte Carlo simulation we will make use of this exact description for the cyclotron movement $\vec{r}(d)$ from Eq. (4.9) [19].

In order to simulate the interaction inside the MCP it is enough to consider one MCP channel, because all channels point in equal directions.
Since the MCP channels come with a bias angle α, one channel can be imagined as a diagonally cut tube (see Fig. 4.2). Hence the MCP channel can theoretically be illustrated by many ellipses lined up in a row (see Fig. 4.3). In original position, the entry ellipse (the first ellipse the electron 'sees' on the way through the MCP channel)

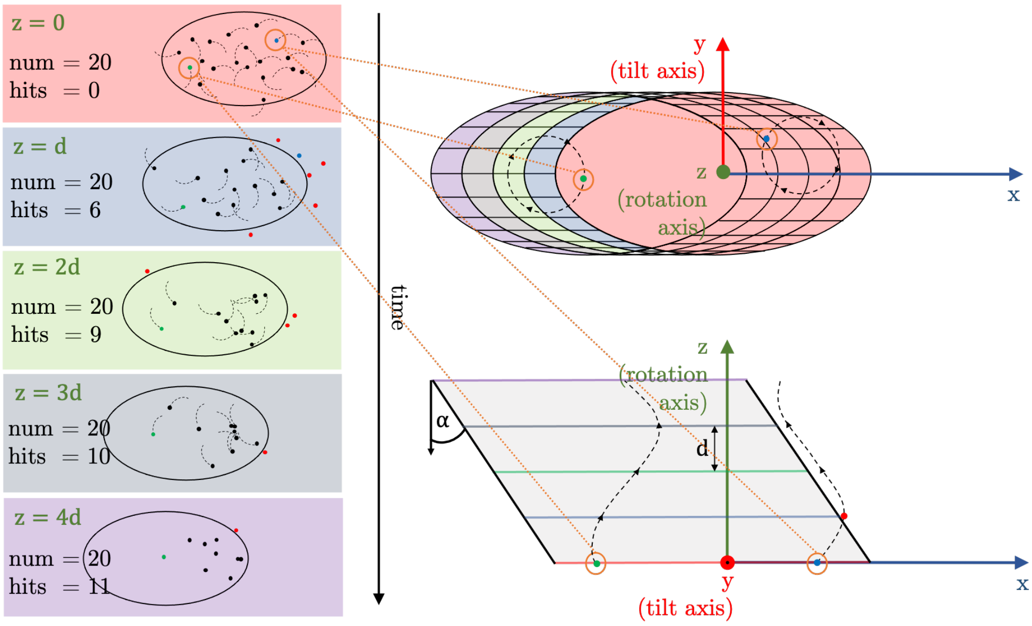

Figure 4.3.: Schematic sktech of the Monte Carlo simulation, simulating num $= 20$ electrons moving on cyclotron tracks inside one MCP channel, which is in original position (tilt angle $= 0°$ and rotation angle $= 0°$) with a bias angle α and a channel depth $D = 4d$. Every electron hitting the MCP channel wall will be counted as hit. The simulation then returns `relative_non_hits`$= 1 - \frac{\text{hits}}{\text{num}}$. In this case the pitch angles θ were chosen randomly with the parameter `phase` being an array of different random values (see Appendix A).

lies inside the x-y-plane ($z = 0$), while the others are stacked in parallel towards the z-axis. Furthermore, these ellipses are shifted by $x_{\text{shift}}(z)$ towards negative values of x in order to reproduce the bias angle.

$$x_{\text{shift}}(z) = -\frac{z}{\tan\left(\frac{\pi}{2} - \alpha\right)} \tag{4.10}$$

For this configuration the tilt and rotation angle of the MCP channel equals zero degrees (see Fig. 4.3).

In the context of this experiment, however it is advantageous to neutralise the bias angle, so that the MCP channel points in z-direction and the electron does not 'see' ellipses but circles. We call that MCP position best possible alignment configuration. This can easily be done by rotating the MCP by the bias angle α around the y-axis (= tilting). The rotational matrix for the MCP tilt $\boldsymbol{R}_y$ with any angle ϕ can then be described as in Eq. (4.11) [20].

$$\boldsymbol{R}_y = \begin{pmatrix} \cos(\phi) & 0 & \sin(\phi) \\ 0 & 1 & 0 \\ -\sin(\phi) & 0 & \cos(\phi) \end{pmatrix} \tag{4.11}$$

For the case of best possible alignment configuration one would prevent the number of channel wall hits to be phase dependent (like in Fig. 4.5) and the only parameter defining the number of hits would be the gyroradius, because a larger gyroradius equals a bigger cross-sectional area orbiting the magnetic field lines and thus results in a higher probability of electron-wall interaction. Such sole gyroradius dependency is intended for the aTEF.

But, since the MCP adjustment is subject to limits as discussed in Chapter 5, it is conceivable that we did not manage to install the MCP exactly with a tilt angle of α and a rotation angle of $0°$ in the beam line. To reproduce the realistic measurement scenario, the simulation therefore features the rotation around the z-axis (= rotation) in addition to the rotation around the y-axis (= tilting). The rotational matrix for the MCP rotation $\boldsymbol{R}_z$ with any angle ψ can then be described as in Eq. (4.12) [20].

$$\boldsymbol{R}_z = \begin{pmatrix} \cos(\psi) & -\sin(\psi) & 0 \\ \sin(\psi) & \cos(\psi) & 0 \\ 0 & 0 & 1 \end{pmatrix} \tag{4.12}$$

In the simulation, these rotations were implemented by tilting and rotating the electron track in inverse direction. This means to use the inverse matrices $\boldsymbol{R}_y^{-1}$ and $\boldsymbol{R}_z^{-1}$ from Eq. (4.13).

$$\boldsymbol{R}_y^{-1} = \begin{pmatrix} \cos(\phi) & 0 & -\sin(\phi) \\ 0 & 1 & 0 \\ \sin(\phi) & 0 & \cos(\phi) \end{pmatrix}; \quad \boldsymbol{R}_z^{-1} = \begin{pmatrix} \cos(\psi) & \sin(\psi) & 0 \\ -\sin(\psi) & \cos(\psi) & 0 \\ 0 & 0 & 1 \end{pmatrix} \tag{4.13}$$

Thereupon the ellipses´ coordinates stay constant. Subsequently, all ellipses are parallel to the x-y-plane independent of ψ and ϕ. In steps of d for negative z values the simulation checks, wether the track coordinate $\vec{r}(d)$ lays inside the ellipse belonging to the corresponding z-coordinate. For a shifted ellipse with a semi-major axis a and a semi-minor axis b applies the following condition (resulting from the standard equation of the ellipse $\frac{x^2}{a^2} + \frac{y^2}{b^2} = 1$), in case the coordinate lays inside. [21]:

$$\frac{(x - x_{\text{shifted}}(z))^2}{a^2} + \frac{y^2}{b^2} < 1 \tag{4.14}$$

Taking into account, that the MCP has a finite channel depth D, one of the three conditions from Eq. (4.15) must be fulfilled.

$$\frac{(x - x_{\text{shifted}})^2}{a^2} + \frac{y^2}{b^2} < 1 \quad \vee \quad z < 0 \quad \vee \quad z > D \tag{4.15}$$

If the condition query of Eq. (4.15) yields **False**, the electron will be counted as hit. It is then assumed, that the electron has hit the MCP channel wall.

The simulation (see `track_particle` function Appendix A) then outputs Eq. (4.16), where num stands for the number of initial electrons generated.

$$\texttt{relative\_non\_hits} = 1 - \frac{\text{hits}}{\text{num}} \tag{4.16}$$

The output thus represents the electrons, which have not hit the MCP channel wall. In order to better compare the results with other tilt angles, it is necessary to have a constant ratio between the area and the number of initial electrons within the measurement series of different tilt angles. This is considered in the `standardized_non_hits` output of the `track_particle` function, which normalises the `relative_non_hits` output to the area of the circle created in best possible alignment configuration.

4.2 Simulation results

The simulation help to better understand the consequences resulting from the geometry of the MCP channels. In Fig. 4.4 **(a)** and **(b)** the symmetry of the MCP is displayed, indicating two best possible alignment configurations in 2α tilt angle distance (tilt angle $= (+/-)\alpha$ and rotation angle $= 0°/180°$). For both cases the MCP channel is parallel to the z-axis. This knowledge will later help us to determine the bias angle α experimentally (see Chapter 5).
Additionally, Fig. 4.4 **(c)** and **(d)** perfectly illustrate the importance of an accurate MCP alignment method. Hence, already with tilt angle deviations of more than $1.5°$ from the $12°$ bias angle, as well as rotation angle deviations of more than $7°$, there is no overlapping area between entry and exit ellipse anymore.
The degree of the MCP alignment will then have an impact on its filter properties. Thus, an obliquely aligned MCP provides a phase effect in terms channel wall hits. Such a phase effect is schematically illustrated in Fig. 4.5 and simulated in Fig. 4.6. While `standardized_non_hits` stays constant over a whole gyroperiod of $360°$ for the MCP being in best possible alignment configuration (just the gyroradius determines the number of `standardized_non_hits`), there is an oscillation in terms of `standardized_non_hits` for configurations deviating from the best possible alignment configuration (see Fig. 4.6). This oscillation increases with the degree of alignment deviation. For a tilt angle deviation of $0.1°$ the graph oscillates with an amplitude of 0.06 around the constant best possible alignment count rate (tilt angle deviation of $0°$). In contrast to that, for tilt angle deviations of $1.5°$ the oscillations´ amplitude is at 0.56 and the count rate being 0 for about two third of the whole period.
In Fig. 4.7 the tilt and rotation angle of the MCP was held constant for different electron pitch angles θ, which in turn belong to different gyroradii via Eq. (4.7). For illustration purposes, the graph only displays the maximum value of its phase sweep

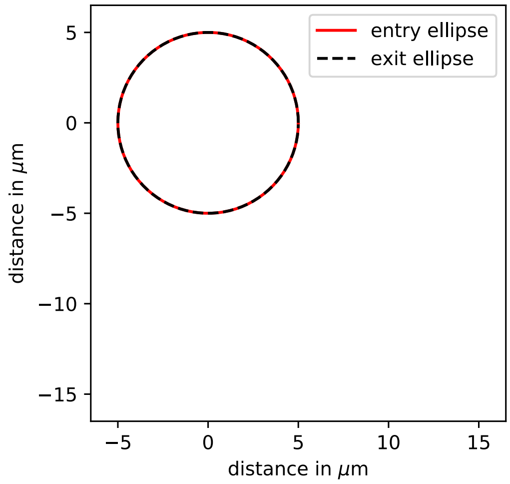

(a) rot. angle $= 0°$ and tilt angle $= 12°$

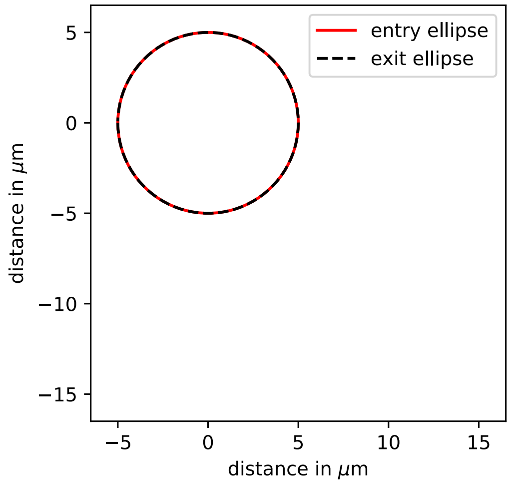

(b) rot. angle $= 180°$ and tilt angle $= -12°$

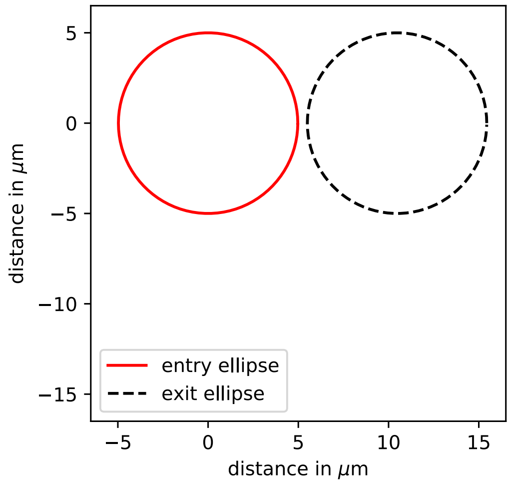

(c) rot. angle $= 0°$ and tilt angle $= 13.5°$

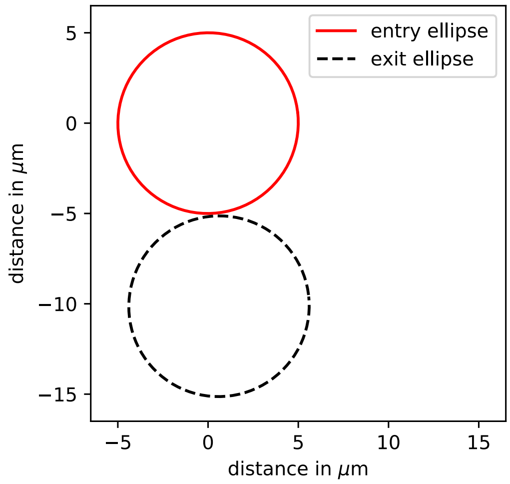

(d) rot. angle $= 7°$ and tilt angle $= 12°$

Figure 4.4.: Simulations of the entry and exit ellipse of the MCP from electron beam perspective. **(a)** and **(b)** show the same configuration and therefore illustrate the symmetry of the MCP. In **(c)** and **(d)** the overlapping area is zero, so that electrons with a gyroradius $r_g = 0\,\mu\text{m}$ would definitely hit the MCP wall. All simulations were performed with an MCP, having a $12°$ bias angle, $400\,\mu\text{m}$ width and channel diameter of $10\,\mu\text{m}$ analogously to the properties of the MCP, we used in the MCP setup of Chapter 3).

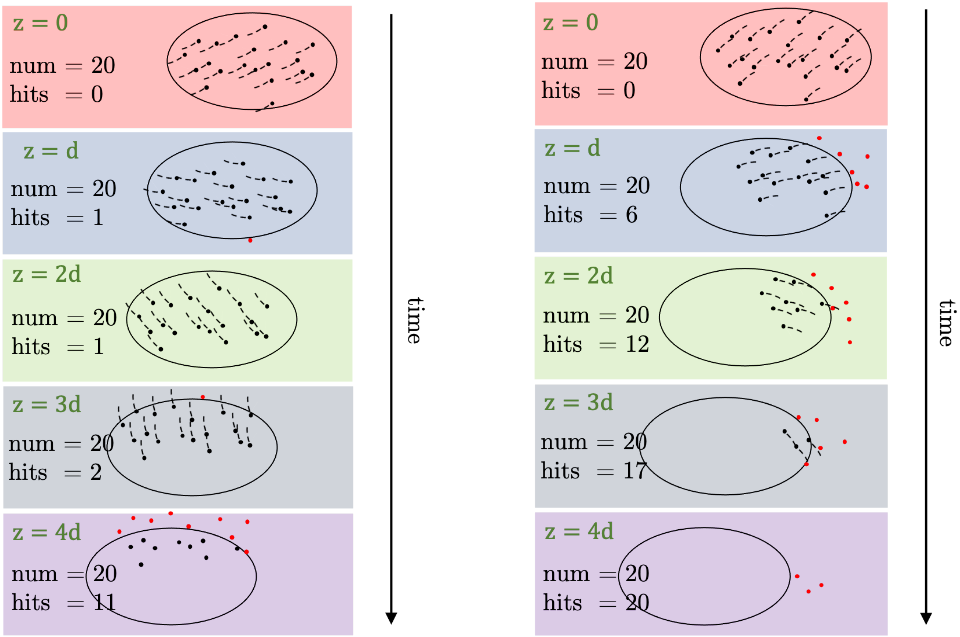

(a) initial electron phase $= \varphi$ **(b)** initial electron phase $= \varphi + 180°$

Figure 4.5.: Schematic sketch of two Monte Carlo simulations **(a)** and **(b)** performed with two $180°$ different initial electron phases. Thus, a phase effect is illustrated, obtaining two different values for the `relative_non_hits` $= 1 - \frac{\text{hits}}{\text{num}}$ of Fig. 4.3 for different starting phases of the electron.

(as in Fig. 4.6). The simulated tilt angle deviation of $1.7°$ is even higher than the $1.5°$ in Fig. 4.4. Analogously, there is no overlapping area as well for the simulations of Fig. 4.7. So if the electron does not move on a rotating path (this is the case for $r_g = 0\,\mu\text{m}$) it has no chance to pass the MCP channel without any channel wall interaction. Consequentially, the distribution has a minimum there. Dropping to zero again for $|\theta| > 3.2°$, the distribution allows passing the MCP channel just for pitch angles $0 < |\theta| < 3.2°$. Plus, the maximum at $|\theta| = 1.8°$ shows, that there is a θ (or r_g), which can best compensate the $2.0°$ rotation and $13.7°$ tilting of the MCP. The distributional shape with two maximums being symmetric around $\theta = 0°$ is identical for other configurations deviating in the magnitude of a few degrees from the best possible alignment configuration. Just the exact values for θ and maximal value of `standardized_non_hits` differ for other MCP configurations. Hence, the graph in Fig. 4.7 is exemplary for other configurations, deviating from the best possible alignment configuration.

These two effects, the phase effect and the dependency of the count rate on the pitch angle θ is expected to measure for realistic alignment scenarios of the MCP. The passive MCP filter measurements of Chapter 6 are conducted, in order to proof this agreement between theory and measurements.

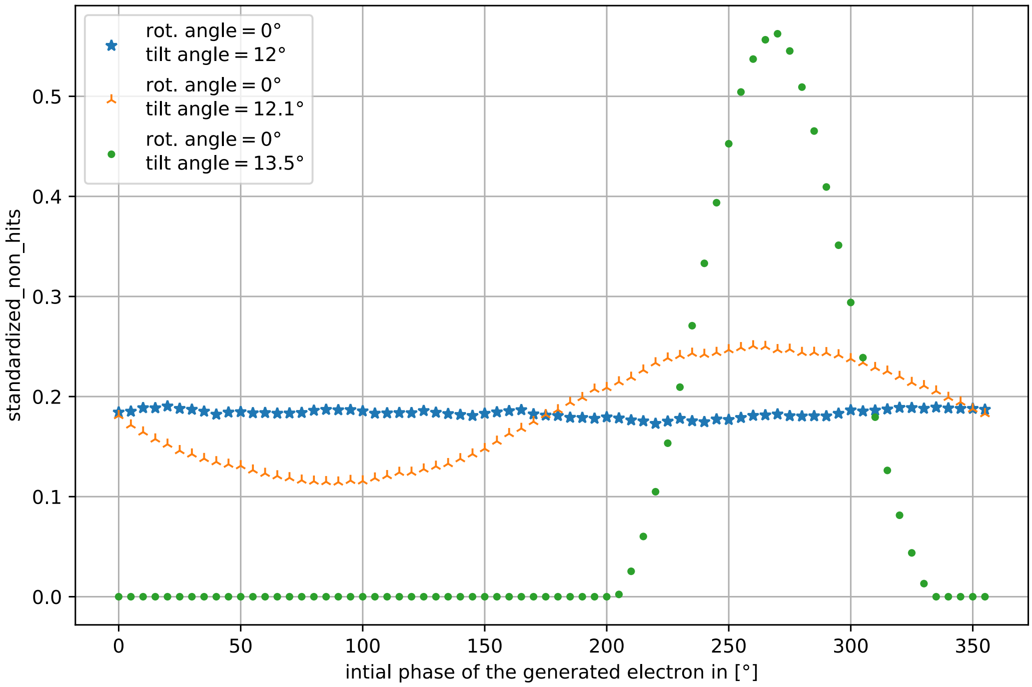

Figure 4.6.: Simulations that illustrate the phase independence of the `standardized_non_hits` for the MCP being in best possible alignment configuration (rotation angle at $0°$ and tilt angle at $\alpha = 12°$) and the phase dependence (phase effect) for deviations from the best possible alignment configuration. All simulations were performed at a pitch angle $\theta = 1°$ resulting in a gyroradius $r_g = 52.4\,\mu\mathrm{m}$ and a period length of $67.0\,\mathrm{mm}$.

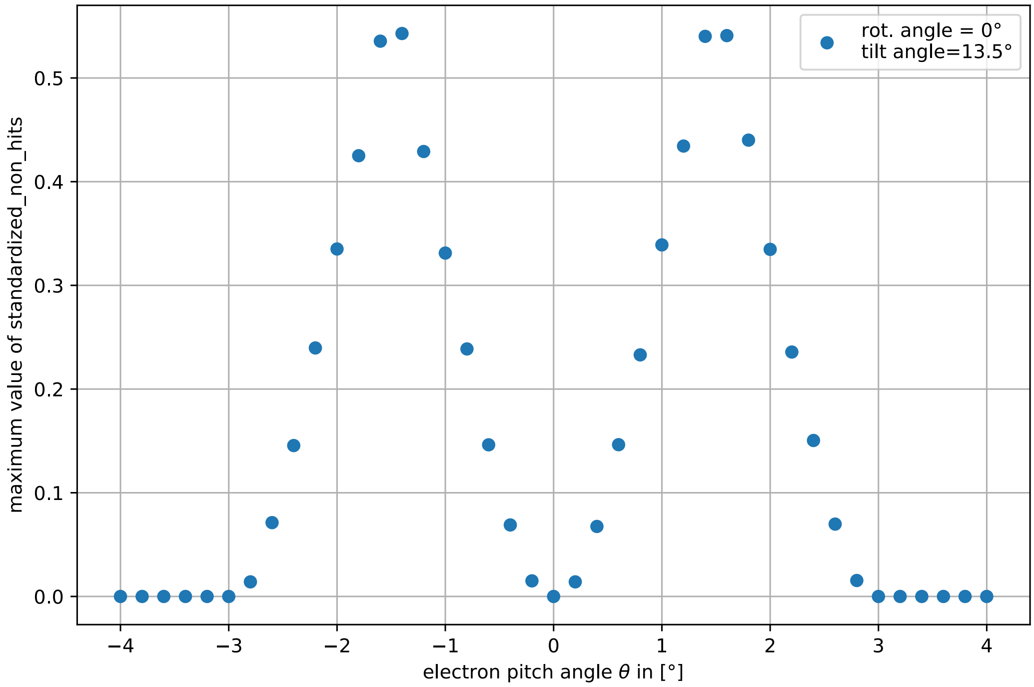

Figure 4.7.: Simulation that illustrates the dependency of the maximum value of `standardized_non_hits` from the electron pitch angle θ, which is via Eq. (4.7) directly connected to the gyroradius $r_g \propto \sin(\theta)$. For a tilted and rotated MCP the distribution is symmetrical around $\theta = 0°$ ($r_g = 0\,\mu\mathrm{m}$). For visualisation purposes, the negative values of the pitch angles θ equal positive polar angles with an azimuth angle shifted by $180°$.

5 Alignment of the MCP filter

In order to investigate wether an aTEF could in principle work it is important to orient the channels of the MCP filter towards the beam tube axis and therefore towards the main magnetic field line of the aTEF test setup. But due to the aforementioned bias angle α of the MCP channels (see Section 3.2) it is not sufficient to place the surface normal of the MCP in line with the beam tube. A method is required, which allows optimal adjustment of the MCP channels without impacting its sensitive SEE layer. For this, one has to take into account the two independent rotation axes of the MCP filter. One axis is represented by the surface normal of the MCP (rotation axis) and one is perpendicular to it, containing the MCP plane (tilt axis).

5.1 Alignment setup

We chose a red laser [1], whose axis shall represent the one of the beam tube from the aTEF test setup. With this laser it is possible to determine the best possible alignment configuration without touching the MCP filter. This non-invasive method enables the protection of the SEE layer. In addition, the diameter of the laser beam is big enough to cover a large number of MCP channels. The resulting interference pattern will then allow us to find the best possible alignment configuration.

To achieve an accurate way of adjusting, we designed a measurement setup on Kanya profiles (see Fig. 5.1). For this, the laser is placed on a laser holding device. The two following iris diaphragms serve as fixation for the beam axis. Once the laser axis is defined, it is possible to return to that original configuration, even if the laser was moved on the laser holder. Going further in the beam path, the laser will then pass the MCP filter that is fixed inside an MCP holding device (MCP holder). This MCP holder is then mounted on two vertically stacked rotators. The adjustable inclined plane under the two rotators guarantees that the laser axis is perpendicular to the tilt axis. In other words: For a tilt angle that equals zero degrees the laser axis is equivalent to the surface normal of the MCP. For intensity analysing purposes, a UV diode, connected to the TPS 2024 oscilloscope from Tektronix, was positioned at the end of the beam path. To investigate the symmetry of the interference pattern by

[1] The wavelength λ is unknown, but plays no role for the MCP alignment, since not the exact dimensions of the interference pattern is of interest, but its symmetry.

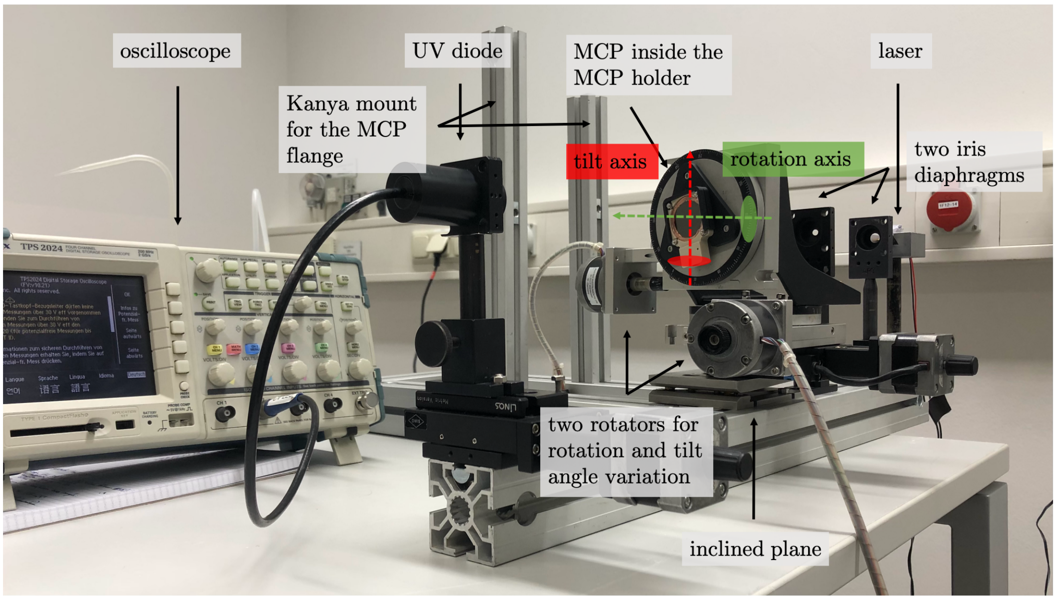

Figure 5.1.: Optical setup for the MCP alignment, before the MCP inside the MCP holding device (MCP holder) will be mounted on top of the MCP flange. In this alignment step (see text) one has to find the ideal rotation angle ψ. Is the MCP holder incl. the MCP holder once mounted on the MCP flange ψ is fixed. This is why the two axes (rotation and tilt axis) shall be varied independently.

eye, the UV diode can be replaced by a screen.

There is a risk of damaging the MCP by rotating it around the rotation axis inside the MCP holder. It is therefore necessary to first determine the optimal rotation angle ψ using the rotator setup, which allows a non-invasive change of ψ. If the optimal rotation angle is found, the MCP can be rotated inside the MCP holder once. In contrast to that, the tilt angle ϕ can later be changed, once the MCP is mounted on top of the MCP flange (see Fig. 5.2). This happens with help of a screw in the range $[11, 13]°$, expecting the bias angle α being around $12°$, as specified by the manufacturer (see Section 3.2.1). With the setup being built with Kanya profiles, it is possible to perform both alignment steps, the one for the optimal rotation angle ψ and the one for the optimal tilt angle ϕ, within the same defined laser axis. Moreover, this setup configuration rebuilds the experimental aTEF setup geometry, with the laser axis representing the electron beam. Consequentially, the set tilt and rotation angle don't have to be modified after the alignment process is completed and the MCP flange is ready to be built into the aTEF setup.

Since preparation work like the soldering of the cables and the mounting itself within the beam tube was performed after the alignment process, slight changes for the fragile construction of the earlier set alignment configuration cannot be excluded. Hence, placing the MCP filter inside the aTEF setup is a source of uncertainties in rotation and tilt angle.

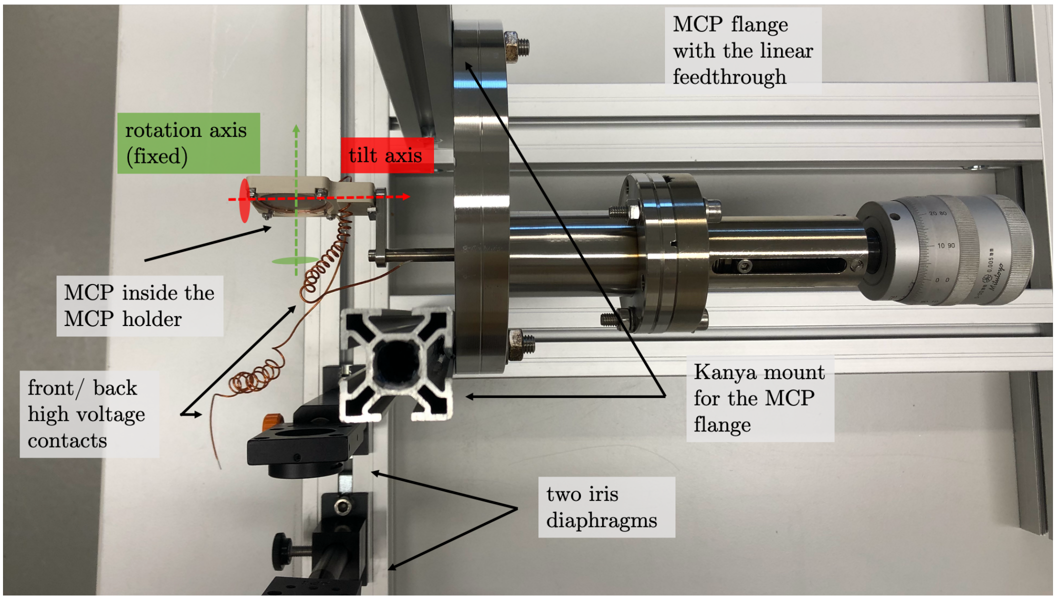

Figure 5.2.: Optical setup for the second alignment step after the MCP filter, placed inside of the MCP holder, was mounted on top of the MCP flange and an optimal rotation angle ψ was found. In this step only the tilt angle ϕ can be changed. Therefore the two rotators from the setup of Fig. 5.1 were replaced by the MCP flange fixated on two Kanya profiles. The other components from Fig. 5.1(not shown in that figure) stay the same. Thus, a geometry analogous to the actual aTEF setup can be rebuilt.

5.2 Theoretical considerations

The MCP is resembling a diffraction object that is a hexagonal lattice, with a lattice constant $a = 12.5\,\mu\text{m}$, consisting of holes with a radius $r = 5\,\mu\text{m}$. The function $f(x, y)$ of that diffraction object can be indicated as the grid function $g_{\text{grid}}(x, y)$, consisting of delta functions at the grids coordinates, convoluted with the aperture function $g_{\text{aperture}}(x, y)$, describing the $5\,\mu\text{m}$ holes:

$$f(x, y) = g_{\text{grid}}(x, y) * g_{\text{aperture}}(x, y) \tag{5.1}$$

The distance $z_0 = (20.7 \pm 0.5)\text{cm}$ between the screen and the diffraction object (in this case the MCP filter) is very large compared to the aperture width $b = 2r \approx 10\,\mu\text{m}$ (in this case the MCP holes). Then the emerging interference pattern can be approximated throughout the Fraunhofer approximation (far field approximation) [22]. In Fraunhofer approximation the electric field $E(x, y)$ on the screen is proportional to the Fourier transform of the real grid function $f(x, y)$. Via the convolution theorem and Eq. (5.1), the following expression thus results for the intensity distribution I [22]:

$$I(x,y) = E^2(x,y) \propto \mathcal{F}^2(f(x,y)) \tag{5.2}$$

$$I(x,y) \propto \mathcal{F}^2(g_{\text{grid}}(x,y) * g_{\text{aperture}}(x,y)) = \mathcal{F}^2(g_{\text{grid}}(x,y)) \cdot \mathcal{F}^2(g_{\text{aperture}}(x,y)) \tag{5.3}$$

The intensity distribution and therefore the interference pattern can, according to Eq. (5.3), be described as the multiplication of the squared Fourier transform of the grid function and the squared Fourier transform of the aperture function.
For the best possible alignment configuration, the aperture function $g_{\text{aperture}}(x,y)$ is given by a pinhole aperture, assuming that the laser then sees a perfect hole. While the squared Fourier transform of the hexagonal grid function $g_{\text{grid}}(x,y)$ is again a hexagonal grid, the squared Fourier transform of a pinhole aperture is given by diffraction discs (that is also shown in the simulation depicted in Fig. 5.3). The resulting overlay of both distributions then produces the interference pattern of the MCP on the screen (see Fig. 5.4).
For tilt angles ϕ deviating a few degrees from the best possible alignment configuration, the grid structure from laser perspective changes minimally, so that the grid constant a is approximately unchanged (because for $\phi \approx 0$ applies $a \cdot \cos(\phi) \approx a$). Analogously there is no change in the maximum positions of the interference pattern in Fig. 5.4 to be expected. In contrast to this, the aperture function changes for tilt angles different from the best possible tilt angle. Then the laser beam does not 'see' a perfect hole and the resulting diffraction disks look different from the ones of Fig. 5.3. Apart from that, the direction of the channels has an influence on the position of origin of the diffraction discs resulting from the aperture function. This leads to a positional wandering of the intensity maximum for different tilt angles (see Fig. 5.5 **(a)**). A reason for this might be reflections inside the channels at the channel walls. Thus, in case the channels point in the same direction as the laser beam, there is a minimum of reflections inside the channel walls. Consequentially, the diffraction disks are expected to be symmetrical around the zeroth order maximum. In fact the whole intensity distribution shall be point-symmetrical around the zeroth order maximum, as displayed in Fig. 5.4. We will use this condition, valid for the best possible alignment configuration, in the following Section 5.3.

Another method of finding the best possible alignment configuration is to directly measure the intensity of the zero order maximum. The assumption is that, for the best possible alignment configuration, reflections inside the MCP are minimal. Then, the loss of energy needs to be minimal as well. As a result, we expect the overall intensity of the interference pattern to have a maximum. Since the intensity distribution of the best possible alignment configuration is symmetrical around the

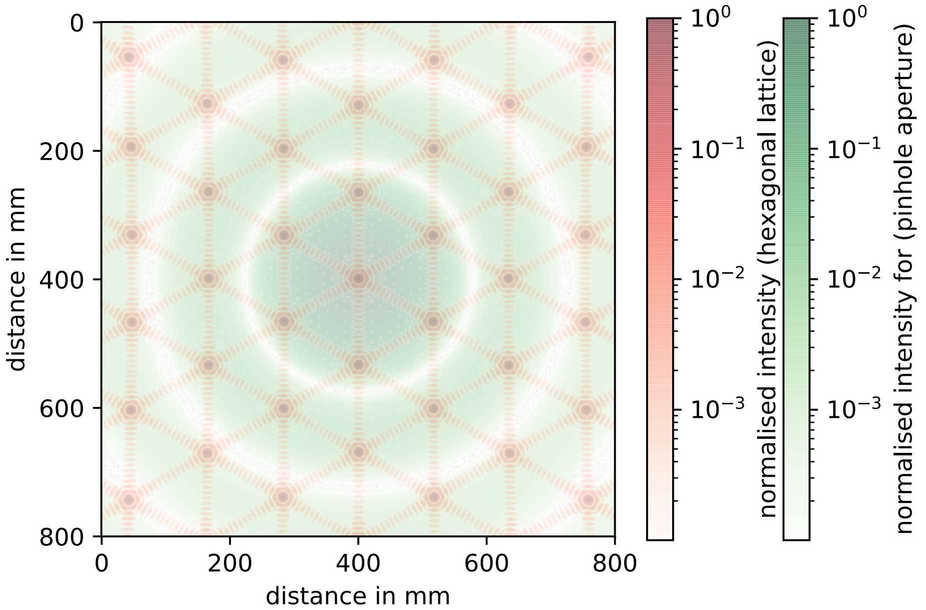

Figure 5.3.: Monte Carlo simulation for visualisation purposes of the intensity for the diffraction at a pinhole aperture (in green) and at a perfect hexagonal grid, consisting of delta function (in red). The distance $z_0 = 20.7\,\mathrm{cm}$ between screen and diffraction object was chosen analogously to the setup parameter in Section 5.1. Likewise the chosen channel radius $r = 5\,\mu\mathrm{m}$ and the grid constant $\mathrm{a} = 12.5\,\mu\mathrm{m}$ (see Section 3.2.1). As wavelength we chose a typical wavelength for a red laser of $\lambda = 700\,\mathrm{nm}$, accepting slight deviations in the dimension of the interference pattern, for the exact wavelength being unknown. The simulation includes 217 grid points. The interference pattern of the pinhole aperture was simulated with 50000 photons going through the aperture and displayed in logarithmic scale to imitate best the intensity perception of the human eye [22]. In order to gain higher contrasts, every pixel with a normalised intensity of less than 10^{-4} was set to zero.

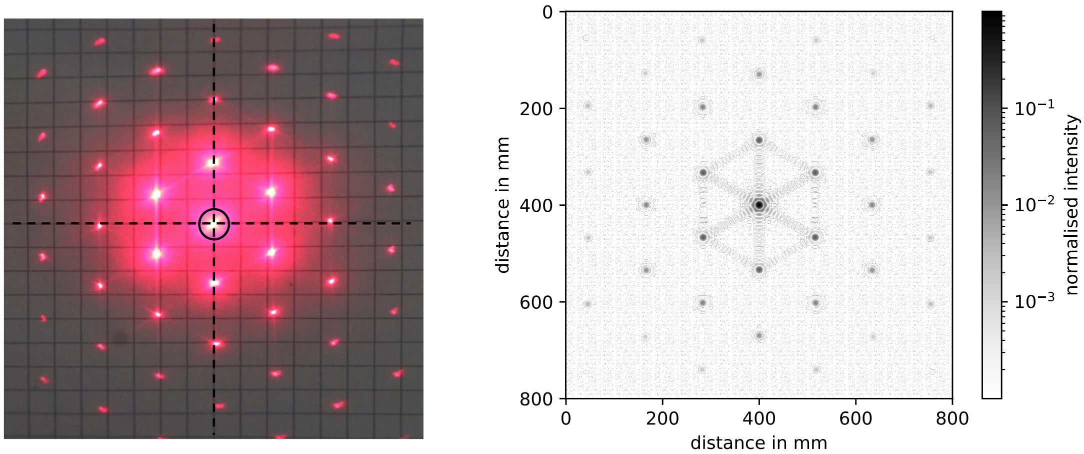

(a) experimental result

(b) simulations result

Figure 5.4.: The experimental result in **(a)** shows a symmetric intensity distribution around the encircled zeroth order maximum with the best possible alignment configuration of $\phi_1 = 1°$ (tilt angle) and $\psi_1 = 348°$ (rotation angle). **(b)** represents the multiplication of the two interference patterns from Fig. 5.3.

zeroth order maximum, it follows that the intensity of the zeroth order maximum has to be maximal for the best possible alignment configuration.

5.3 Intensity and symmetry measurements

In the upper graph of Fig. 5.5 **(b)** the intensity distribution of the zeroth order maximum, that lies in the coordinate origin of all photos, for different tilt and rotation angles of the MCP filter is shown. In contrast to the theoretical considerations of Chapter 4, the original position of the MCP is unknown. Consequentially ϕ and ψ from the rotator setup are relative values for the respective angles. By eye we determine the tilt angle ϕ_1 of the intensity maximum to be within the blueish area. For conventional reasons, we specify the mean value of ϕ_1 in the center of the blueish area. Consequentially the uncertainty $u(\phi_1) = 0.6°$ results as half of the width of the blueish area. The rotation angle of the best possible alignment configuration ψ_1 is represented by the green measurement points, taking into account that the intensity maximum for the intensity distribution has to be maximal. That has to apply analogously for the measurement points, which are shifted by $180°$ in rotation angle, assuming the geometrical symmetry of the MCP, discussed in Chapter 4. So we specify the uncertainty to be $u(\psi_1) = 2°$ (the distance in rotation angle ψ between the measurement points). This guarantees in both cases, the unshifted and the shifted intensity measurements (represented by the upper and the lower graph of Fig. 5.5 **(b)**), that one of the three green measurement distributions has the greatest intensity. For convention reasons the mean value of ψ_1 is represented by the mean of the three green intensity distributions. The values for ϕ_1 and ψ_1 are then given as below:

$$\phi_1 = (1.0 \pm 0.6)°$$
$$\psi_1 = ((168 + 180) \pm 2)° = (348 \pm 2)°$$

The photos of Fig. 5.5 as well suggest a symmetrical intensity distribution of the interference pattern around the zeroth order maximum for ϕ_1. This indicates the similarity of the two proposed alignment methods from Section 5.2.
Taking into account that, by rotating the MCP around $180°$, the geometry of the MCP allows two best possible alignment configurations (see chapter Chapter 4), a second optimal tilt angle ϕ_2 can be found (see lower graph of Fig. 5.5):

$$\phi_2 = (25.2 \pm 0.6)°$$

As described in Section 4.2 half the difference between these two optimal tilt angles ϕ_1 and ϕ_2, then determine the bias angle α_{exp} of the MCP filter.

$$\alpha_{\text{exp}} = \frac{|\phi_2 - \phi_1|}{2} = (12.1 \pm 0.4)^\circ$$

This experimental value for the bias angle fits the one indicated by the manufacturer of $\alpha_{\text{theo}} = 12^\circ$ (see chapter Section 3.2.1) within the error limits.
With respect to this rotation symmetry of the MCP filter one would expect a similar shape of the intensity distributions, which differ 180° in rotation angle (see Fig. 5.5). But in the lower graph, the measurement points for tilt angles of more than 26° deviate from this supposition. This can be justified by the setup design, which does not allow the entire laser beam to hit the MCP filter for tilt angles of more than 26°. Consequentially, there is a systematic intensity loss starting from 26°.

5.3.1 Methodical limits

Another comment concerns the uncertainties of the tilt and rotation angle. By means of alternative alignment methods, such as the direct symmetry measurement (i.e. measurements of intensity difference for higher order maximums), one can in principle obtain much more precise values for the optimal tilt and rotation angles. But design limits for the MCP filter adjustment on the MCP flange restrict the accuracy, with which the determined rotation and tilt angle can be set. The rotation of the MCP filter inside the MCP holder can only be done with an uncertainty of around 5°. Plus, the screw at the top end of the MCP holder only allows tilt angle modifications with an uncertainty of around 1°. It is therefore unnecessary to perform more sophisticated measurements in order to get a more precise determination of the optimal tilt and rotation angle.
Nevertheless the simulations in Chapter 4 have shown, that even for tilt angle deviations of more than 1° from the best possible alignment configuration, the MCP filter should work as electron multiplier, even though the SEE is dependent on the gyrophase of the electron. This phase effect is investigated by measurements in the following Chapter 6.

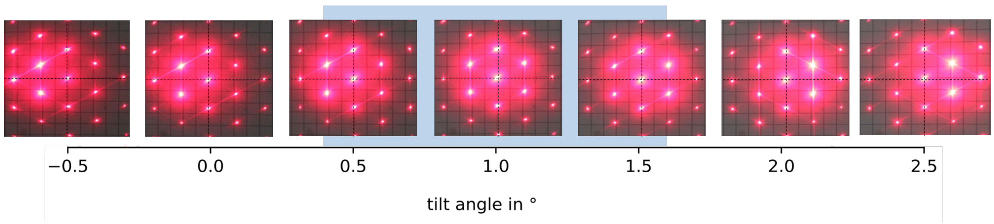

(a) symmetry measurements at 348° (= 168° + 180°) rotation (rot.) angle

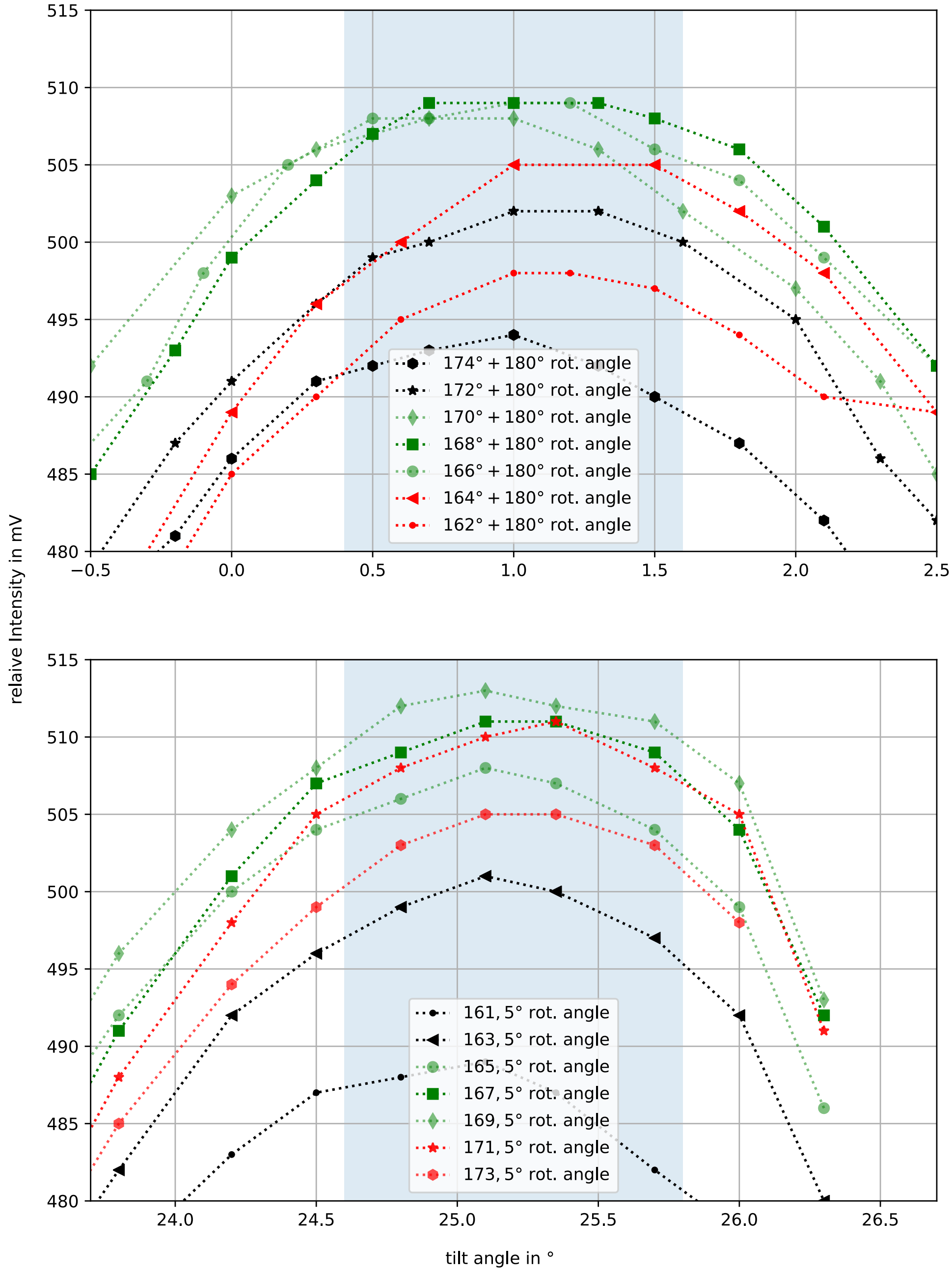

(b) zeroth order intensity measurements at different rotation (rot.) angles

Figure 5.5.: In **(a)** photos show the movement of the intensity distribution for the interference pattern of the MCP filter with respect to the tilt angle (fixed rotation angle of 348°). The intensity is symmetric around the center (= zeroth order maximum) at 1°. In **(b)** intensity measurements for different rotation angle are shown, indicating a maximum in relative intensity for 1° tilt angle and 348° rotation angle (best possible alignment configuration). Error bars smaller than symbols.

6 Passive MCP filter measurements

In this chapter the MCP filter in the aTEF test setup from Chapter 3 is operated passively. That is to say that no differential voltage between MCP front and back is applied. Electrons hitting the MCP wall will thus not generate secondary electrons. In this configuration it is possible to approximately immitate the simulations from Chapter 4.
Those passive MCP filter measurements are necessary in order to better classify the SEE abilities, for the MCP filter operating in active mode with applied differential voltage.

6.1 Gyrophase dependence on the electron transmission

Is the MCP not perfectly parallel to the B-field direction, one can assume, that there is a gyrophase dependency in count rate (phase effect) as discussed in Chapter 4. In other words, electrons with a certain gyrophase have a higher probability to pass through the MCP filter without MCP-wall-interaction. In this case the electron passes the filter nearly parallel to the MCP channels. As discussed in Section 5.3.1 it is unlikely that we placed the MCP filter in perfect concordance within the main magnetic field line. Consequentially a variation of the gyrophase is necessary to proof that electrons can pass the MCP filter without wall interaction.

For the following measurements, it was essential to find a setup parameter configuration, that allows many electrons to pass the MCP filter. We achieve this for a polar angle of $(4.01 \pm 0.05)°$ and an azimuth angle of $(149.55 \pm 0.05)°$ at the Egun plate (see Egun tilt angle α_p from Fig. 3.2), with a current at beam coil 1 of $(5.0 \pm 0.1)\mathrm{A}$ [14].
There are two different methods applied to change the gyrophase of the electron, when the electron is entering the MCP filter. Firstly, there is the possibility to change the beam coil 1 current (see Section 6.2). Another way to do so, is to vary the azimuth angle of the Egun plate. This second method is the more intuitive one, because the azimuth angle marks one point on an imaginary circle at a defined Egun polar angle. This point then represents the starting position of the cyclotron motion. On this imaginary circle the angle between magnetic field lines and the longitudinal

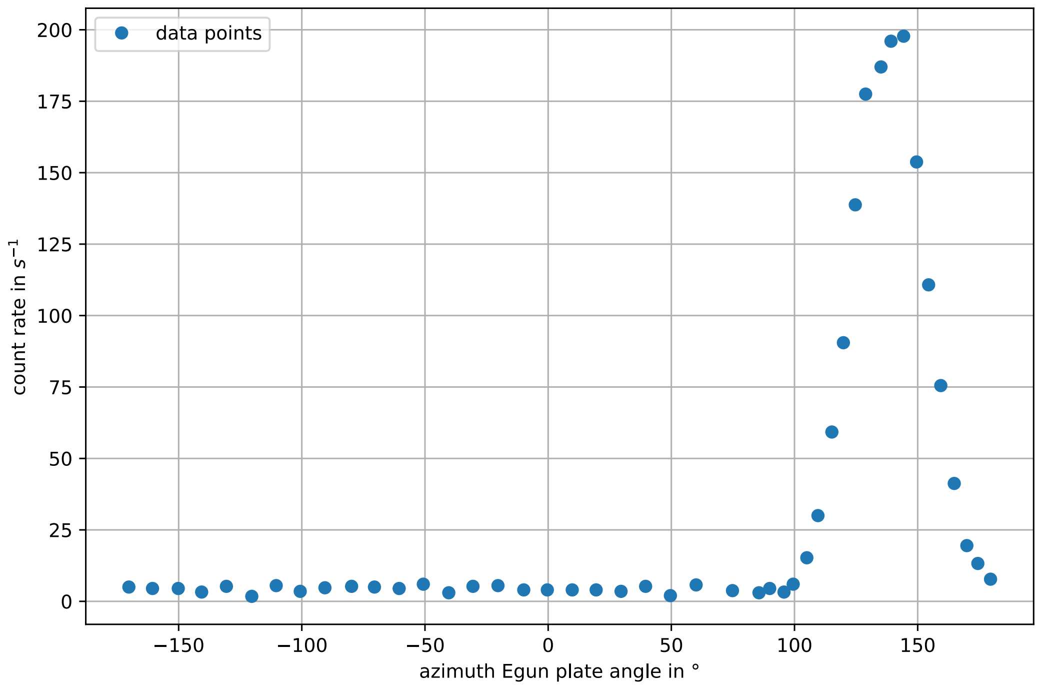

Figure 6.1.: Measurement of azimuth angle variation for the Egun plate being at a constant polar angle of $(4.01 \pm 0.05)°$ and a constant beam tube 1 current of $5.0 \pm 0.1)\mathrm{A}$ with the MCP in beam line. Error bars smaller than symbols.

component of the electron movement is constant, while the transverse component rotates analogously to the azimuth alteration (only applies for a perfect concurrency between magnetic field lines and the longitudinal direction of the electrons). If one varies the azimuth angle around $360°$ it is therefore possible to simulate a gyrophase variation of exactly one period. This method only works because the hole in the Egun front plate rotates, while the pivot point is at the Egun back plate.
This variation of azimuth angle at a constant polar Egun plate angle is shown in Fig. 6.1. While between $(99.470 \pm 0.05)°$ and $(180.550 \pm 0.05)°$ there is a peak in count rate up to $200\,\mathrm{cts/s}$, one can observe a constant background noise below $6\,\mathrm{cts/s}$ for the remaining azimuth angles. There, all electrons seem to hit the MCP Filter wall, so that no signal electron reaches the MCP detector. The MCP detector then outputs the lead glass intrinsic dark count rate as well as other background components.

Comparing the measurement from Fig. 6.1 with one that was made without the MCP filter in the beam line at equal setup parameters permits us to further verify the experimental results of the MCP filter phase effect. In Fig. 6.2 one can as well observe a variation in count rate with respect to the azimuth angle, that originates from the MCP detector phase effect. The count rate peaks at $(39.620 \pm 0.05)°$ with up to $569\,\mathrm{cts/s}$ and goes down to $369\,\mathrm{cts/s}$ for an azimuth angle of $166.440 \pm 0.05)°$. In contrast to the measurements of Fig. 6.1, the peak region of that phase effect is

effectively larger and extends nearly over the whole period length.
A reason for such a gyrophase dependent phenomenon without any MCP filter in beam line can be found in the MCP detector design, which consists of two single MCP plates in chevron stack (see Section 3.2.2). Because of the comparable geometry of the single MCP detector plates and the MCP filter plate, it is to expect the electrons for certain angles to pass through the first MCP plate of the MCP detector without wall interaction as it is the case for MCP filter measurements from Fig. 6.1. This is to say, that not every signal electron entering the MCP detector will be detected in the first MCP. But the probability of a sufficient secondaries generation inside the MCP detector that leads to a discriminator pulse, shrinks with the depth of the electron-MCP-wall-interaction. Consequently, the count rate is about to drop at these azimuth angles.
The widening of the peak region from Fig. 6.2 in contrast to Fig. 6.1 can be a consequence of a slightly different channel direction. The MCP detector was placed on a slanted CF100 flange in order to neutralise the bias angle of the first MCP detector plate, as mentioned in Section 3.2.2. Even though both, the channels of the MCP filter and the ones of the front plate of the MCP detector shall point in the direction of the B-field, there might be deviations of the exact channel direction due to uncertainties in the alignment processes (see Section 5.3.1). The simulations from Fig. 4.6 show that the distribution width of the phase effect changes for different non-ideal alignment configurations. So this could be a justification for the widened distributional shape of Fig. 6.2.
Nevertheless one can state, that there is no direct correlation in between the phase effect of the MCP filter (see Fig. 6.1) and the one of the MCP detector (see Fig. 6.2). First the count rate peaks lay at two totally different azimuth angles. Secondly, the count rate for the MCP filter equals noise rate level below $6\,\mathrm{cts/s}$ for most of the azimuth angles, while the MCP detector counts at all azimuth angle at least $370\,\mathrm{cts/s}$. The only region of a possible overlay between both phase effects, can be found in the area between $(99.470 \pm 0.05)°$ and $(180.550 \pm 0.05)°$. There the count rate of the MCP filter measurement is greater than noise rate level. For that reason, the shape of the count rate distribution for the MCP filter could be slightly different without a phase sensitive detector. But this influence can nearly be neglected, because of the count rate change for the MCP filter phase effect being more than a magnitude greater than the change of the MCP detector phase effect.

It can thus be said, that we measured a gyrophase dependency for the MCP filter placed in beam line. This phase effect looks similar to the simulated phase effect of an MCP filter, which tilt angle is misaligned by $1.5°$. On the one hand, this can be seen as a confirmation of the underlying theory of electron motion and MCP geometry. On the other hand, it can also be assumed that the MCP channel direction is not in perfect concordance with the main magnetic field line.

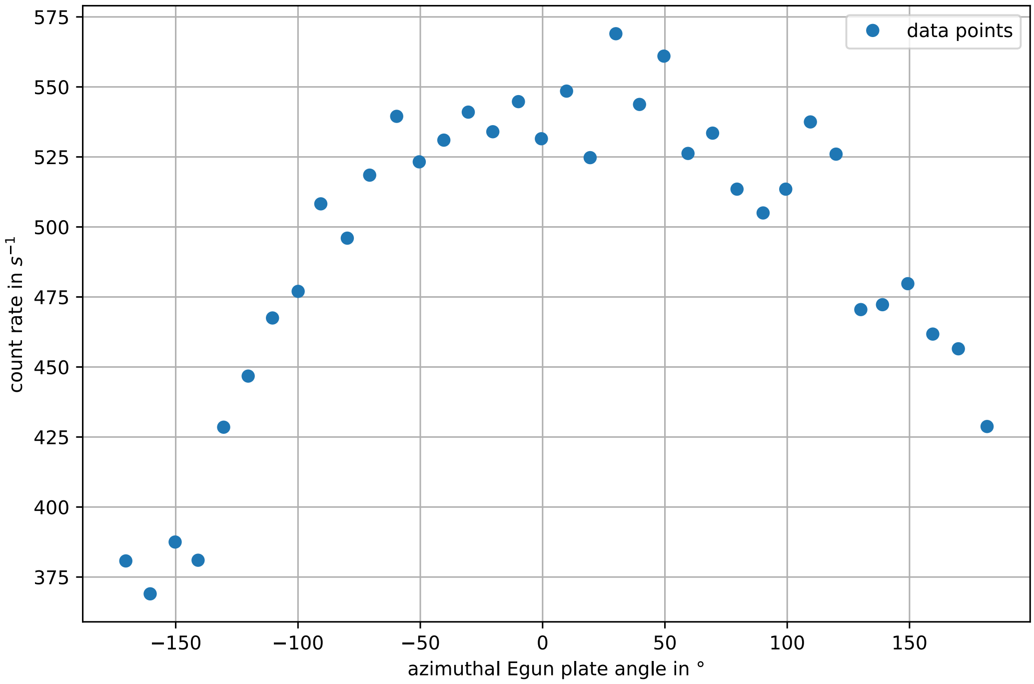

Figure 6.2.: Measurement of azimuth angle variation for the Egun being at a constant angle of $(4.01 \pm 0.05)°$ and a constant beam coil 1 current of (5.0 ± 0.1)A without the MCP filter in beam line. Error bars smaller than symbols.

6.2 Gyroradius dependence on the electron transmission

Alternatively, the gyrophase of the electron can be modified with help of the current at beam coil 1. This beam coil current variation is automatised with a LabView program developed by P. Oelpmann, which permits a faster measurement. For constant Egun tilt angles α_p, one can obtain a count rate distribution similar to Fig. 6.1, but over multiple periods (see Fig. 6.3). A disadvantage of that method only poses the precision in terms of phase information. Against this, the azimuth angle method, as described in the previous section, is the more accurate one.

A theoretical description of the current change dependency on the gyrophase is needed, in order to justify that method. Therefore Eq. (4.6) from Chapter 4 yields the period length T with respect to the magnetic field strength $|\vec{B}| = B$:

$$T = 2\pi \cdot \frac{m_e}{e \cdot B} \tag{6.1}$$

For beam coil 1, the magnetic field strength B inside vacuum can be approximated throughout Eq. (6.2), with $n \approx \frac{1}{2.19}$ mm^{-1} denoting the winding density, μ_0 representing the magnetic field constant and I the coil current [22].

$$B \approx \mu_0 \cdot n \cdot I \tag{6.2}$$

For the performed measurements, the electron has a kinetic energy of $E_e = 1\,\mathrm{keV}$, neglecting relativistic effects like it was done in Chapter 4. For Egun tilt angles α_p of a few degrees, as it is the case for the considered measurements, the longitudinal energy $E_\| = \cos^2(\theta) \cdot E_e$ can be approximated as $E_\| \approx E_e$. Considering the non-relativistic longitudinal kinetic electron energy $E_\| = \frac{1}{2} m_e v^2 = \frac{1}{2} m_e \frac{s^2}{t^2}$ as in Eq. (4.1), gives the time t it takes for the electron to pass the beam coil 1 with a winding length $s \approx 103.6\,\mathrm{cm}$:

$$t \approx \frac{s}{\sqrt{\frac{2E_\|}{m_e}}} \tag{6.3}$$

For t being exactly one period length ($t = T$), the current I_theo can be calculated as in Eq. (6.4), using Eq. (6.1), Eq. (6.2) and Eq. (6.3).

$$I_\text{theo} \approx \frac{2\pi \cdot m_e \cdot \sqrt{\frac{2E_\|}{m_e}}}{s \cdot e \cdot \mu_0 \cdot n} = 1.12\,\mathrm{A} \tag{6.4}$$

I_theo then approximately describes the absolute current change it takes to modify the gyrophase of the electron by one period.
Via Fig. 6.3, the current I_exp of a gyroperiod can be determined experimentally as the mean value of all distances between the maximum count rate values.

$$I_\text{exp} = (1.01 \pm 0.06)\mathrm{A} \tag{6.5}$$

Taking into account, that I_theo is a rough estimation, requiring perfect vacuum conditions and no electric energy loss during propagation, I_exp suggests a confirmation of this theoretical considerations. Varying the current of beam coil 1 is therefore a justified method, in order to change the phase of the cyclotron motion at the MCP filter entry.

In Fig. 6.3 one can identify an effect on the count rate maximums for different polar Egun plate angles, where the maximum positions stay the same. It is therefore not a phase shift of the electrons, which effects the count rate shape, but the gyroradius r_g, which is proportional to $\sin(\theta)$ and therefore directly connected the Egun tilt angle α_p (polar Egun plate angle). For a more detailed description of this phenomenon the reader is referred to Chapter 4.
Another observable effect from Fig. 6.3 is the alternation of count rate maximums during one measurement for a constant polar Egun plate angle. The reason for this

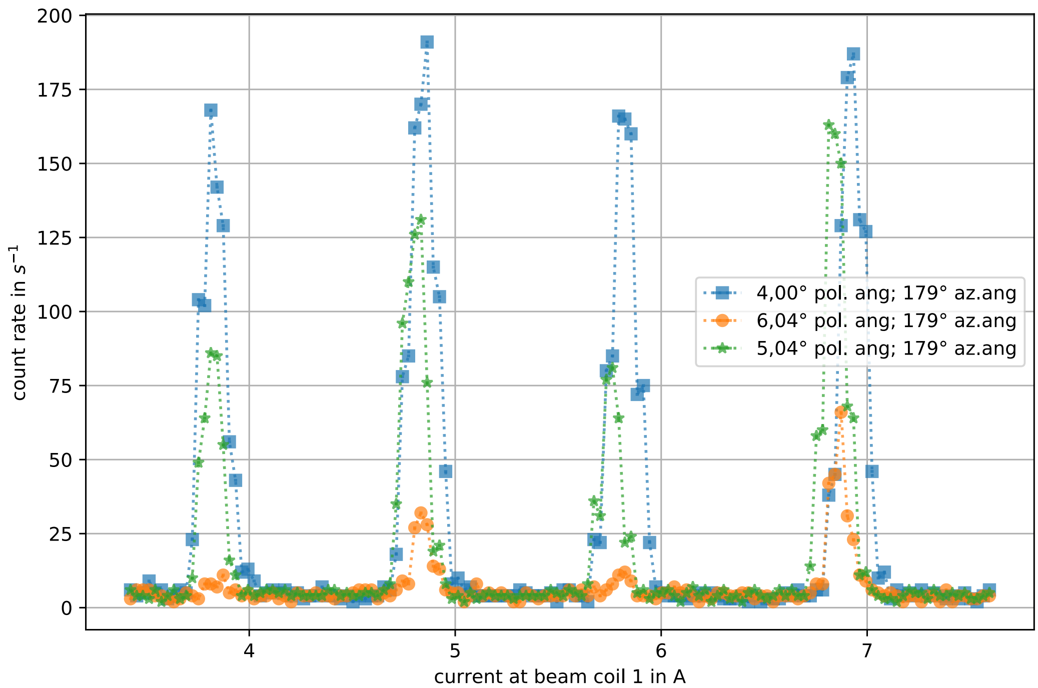

Figure 6.3.: Current variation at beam tube 1 for different polar Egun plate angles. Error bars smaller than symbols.

could be the mentioned imprecise phase resolution of that chosen current sweep method. But an inhomogeneous magnetic field inside the MCP filter, as well as a deviation from the demanded parallelism in between the magnetic field and the original Egun axis ($\alpha_p = 0°$) could cause such a phenomenon too.
To further analyse the Egun tilt angle (polar Egun plate angle) dependency on the transmission probability of the MCP filter one has to extract only the peak height information. To do so and in consideration of the periodical difference of the count rate maximum, we determine the mean value of all count rate maximums (see Fig. 6.3). Since we do not know the function, describing the distributional shape of the peaks, we only picked the maximal value for every of the four peaks. The resulting graph is shown in Fig. 6.4. It indicates a symmetric distribution of count rate maximums around the $-1°$ polar Egun plate angle. For $-1°$ the distribution has its minimum with $17\,\mathrm{cts/s}$. At $-4°$ with $178\,\mathrm{cts/s}$, respectively at $2°$ with $159\,\mathrm{cts/s}$ the distribution reaches its climax until it falls again towards its borders at $-7°$, respectively at $5°$.
This double peak distribution of Fig. 6.4 is expected, if the MCP filter channels are not perfectly parallel to the main magnetic field line. In that case electrons with a gyroradius equals 0 will probably not have the chance, to directly pass the MCP filter (see Chapter 4 for further explanation). This one can observe for a polar Egun plate angle of $-1°$, assuming that electrons then have a gyroradius equals 0. For bigger polar Egun plate angles the passing probability at a certain phase rises until it reaches its maximum at $-4°$ and $2°$, where the angle of the cyclotron motion induces

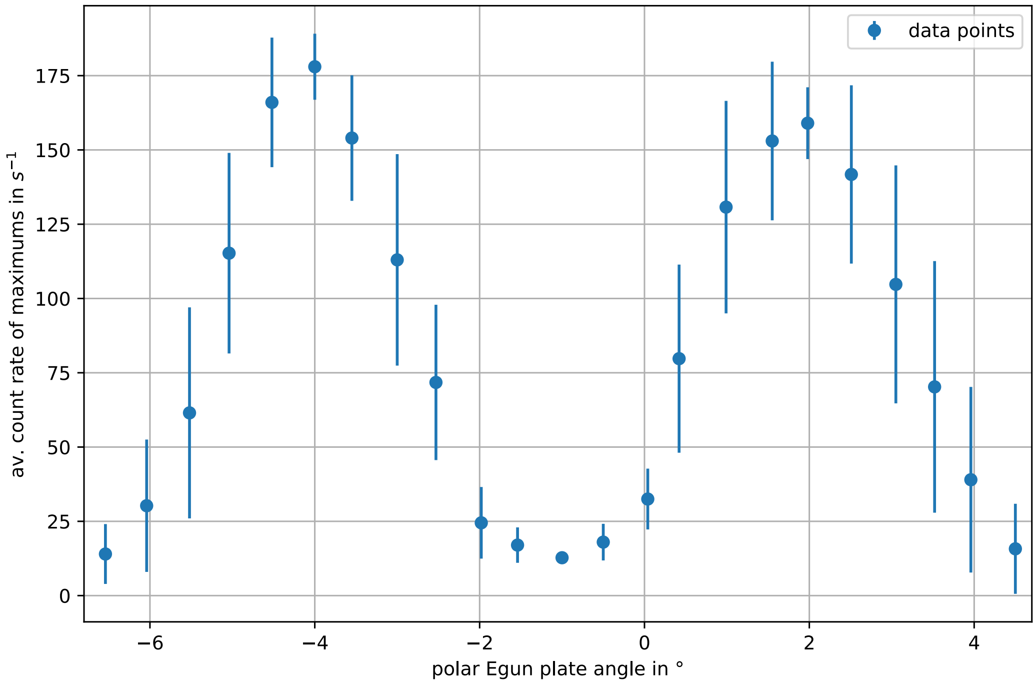

Figure 6.4.: Mean value of all 4 periodical maximums (see Fig. 6.3 for different polar Egun plate angles). For visualisation purposes, the negative values of the polar Egun plate angle, equals positive polar angles with an azimuth angle shifted by $180°$.

an electron propagation nearly parallel to the MCP channels. For even bigger polar Egun plate angles, the passing probability then drops again. A similar shape, but with different angles are obtained from the simulations of Fig. 4.7. Deviations result from the unknown exact alignment of the MCP filter channels and from the fact that the simulations in Chapter 4 are subject to strong idealisations of the actual aTEF setup. Thus, with equation Eq. (3.4) and the lack of knowledge about the scaling factor k, the exact relation between electron pitch angle θ and Egun plate angle α_p is not taken into account. Additionally, the simulation does not consider the exact B-field strength at the Egun as well as the adiabatic transport of the electron between its generation at the Egun and the MCP filter. Simplified, the simulation assumes that the B-field at the filter is the same as at the Egun. But, because of the shape concordance, the measurement once again qualitatively confirms the underlying theory of electron motion and MCP geometry, which is implemented in the simulation of Chapter 4.

Furthermore this experimental outcome might indicate an inclination between the original Egun axis and the main magnetic field line at the Egun of around $1°$. That would be an explanation for the distribution of Fig. 6.4 being symmetric around $-1°$. One reason for the inclination could be the helical winding of the beam coil 1, resulting in unhomogeneous magnetic field lines at coil entry and exit as displayed in Fig. 6.5. Since the entry of beam coil 1 is located near the Egun, that might also affect the pitch angle θ of the electrons and therefore its gyroradius. Another justification

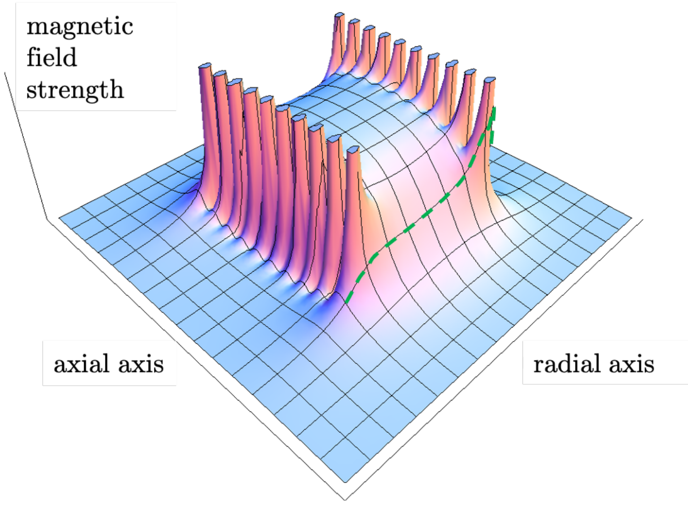

Figure 6.5.: Magnetic field of a cylinder coil of ten windings, with the slice plane going axial through the coil center. The green dashed line exemplary marks an inhomogeneity at the entry or exit region of the coil. The figure was modified from [23].

of the distributional shift by $1°$ could lay in a slight misalignment between beam tube axis and Egun.

Nevertheless, we can state that the aTEF setup allows the modification of gyroradii and thus imitate signal and Rydberg induced electrons, which are characterises by its difference in gyroradii.

7 Active MCP filter measurements

This section is subject to the active MCP filter measurements, making use of its SEE properties, in case an electron hits the activation layer and a differential voltage between MCP front and back is applied. In order to perform the proof of working principle for the aTEF, we aim for a separation between single Egun electrons (signals) and the avalanche of secondary electrons (secondaries), which will be released after a signal electron has hit the MCP channel wall.

7.1 Preparatory experimental considerations

To proof the success of such a separation between single and secondary electrons, it is necessary to compare passive and active MCP filter measurements. Permitting a comparison between passive and active measurements, the electron shall perform a similar cyclotron motion throughout both measurements. The electric potentials, the electron 'sees' after generation at the Egun, are displayed in Table 7.1 for active MCP measurements. Since electric potentials influence the kinetic electron energy and

Table 7.1.: Overview of electric potentials for active MCP measurements. The electron is affected by these after being generated on ground potential with a kinetic energy of $1\,\mathrm{keV}$ at the Egun. For further description see Section 3.2.1.

	MCP filter front	MCP filter back	MCP detector	MCP detector back
Voltage in V	-750	-50	0	1853

thus affect the cyclotron motion parameter, it is to chose a similar potential setting for the passive MCP measurements. But passive measurements are characterised by the fact that no differential voltage between MCP front and back is applied. This means that the potential difference is $0\,\mathrm{V}$. Consequentially, there is per definition a difference in terms of electric potentials between active and passive measurements. The configuration of electric potentials, which reproduces best the one of the active MCP measurements is shown in Table 7.2. For this configuration the electron 'sees' exactly the same electric counter field as for the active measurements until it reaches the MCP front. This is of importance, in order to have equal passing conditions, when the electrons enter the MCP filter. Inside the MCP the electric potentials for passive and active measurements then differ. But assuming a short acceleration

Table 7.2.: Overview of electric potentials for the passive MCP measurements in this section. The electron is affected by these after being generated on ground potential with a kinetic energy of $1\,\mathrm{keV}$ at the Egun.

	MCP filter front	MCP filter back	MCP detector	MCP detector back
Voltage in V	-750	-750	0	1853

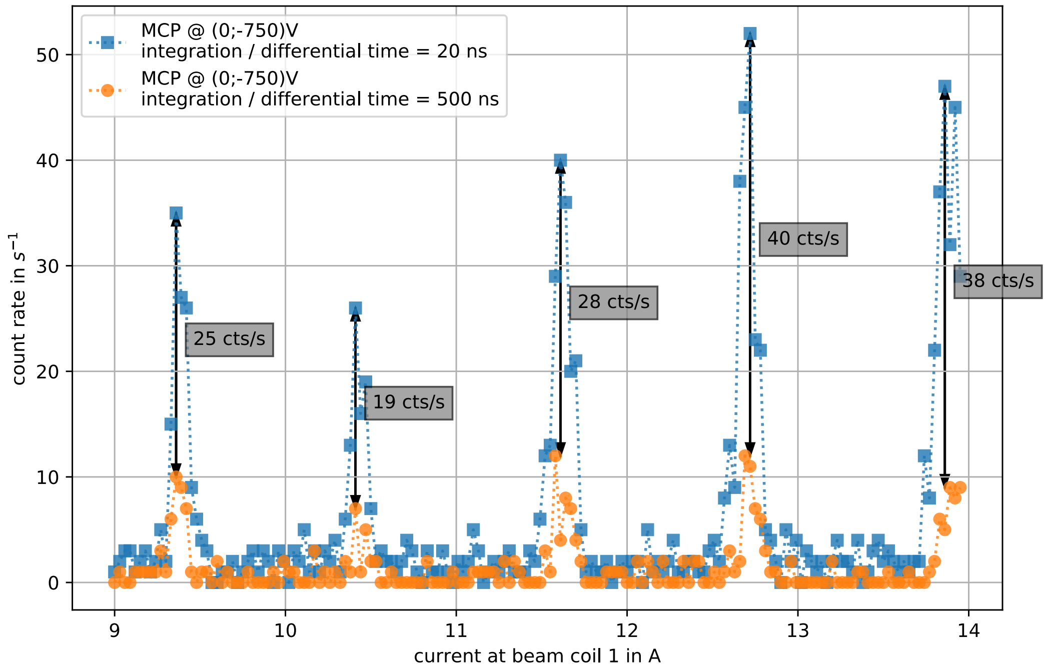

Figure 7.1.: Phase sensitive variation of the beam coil 1 current for the passive MCP filter with an integration/differential time of $20\,\mathrm{ns}$ and $500\,\mathrm{ns}$ at the TFA, aiming for a suppression of the single signal electrons. The MCP filter has been operated at a differential Voltage of $0\,\mathrm{V}$ and at a reference Voltage of $-750\,\mathrm{V}$ (MCP @ $(0;-750)\mathrm{V}$). Error bars smaller than symbols.

track in the size of the MCP filter channel depth ($400\,\mu\mathrm{m}$), the influence of the exact electron track coordinates inside the MCP is estimated to play no major role, even though it is not negligible.
This considerations allow us to have comparable MCP filter transmission probabilities for passive and active measurements, if electrons are generated at an equal gyrophases. Once the electron has left the MCP filter, a cyclotron motion equality is not of importance any more, because we first assume, that nearly every electron, regardless of its cyclotron motion parameters, gets multiplied in the MCP detector. Thereupon a difference in terms of electric potentials for the section between MCP filter back and MCP detector front is irrelevant.

Aiming for a separation between the electron avalanche and single electrons, one has to find a setting with which the electron avalanche will be counted as one, while the single electron will be counted as zero at the pulse counter. The TFA shall therefore serve as threshold filter. For this, we performed a phase sensitive sweep of the beam coil 1 current with the MCP filter in passive mode for $20\,\mathrm{ns}$ and for $500\,\mathrm{ns}$ of integration/differential time. During these measurements the MCP was set on potentials, mentioned in Table 7.2. By changing the TFA integration/differential time from $20\,\mathrm{ns}$ to $500\,\mathrm{ns}$, a single electron suppression of more than $(80.5 \pm 7.9)\%$ can be reached (see Fig. 7.1). This means, that the count rate at the peak regions from Fig. 7.1 decreases on average by $(80.5 \pm 7.9)\%$ for the higher integration/differential time. To obtain the mentioned percentage value for single electron suppression, it is to determine the average ratio of count rate difference and absolute count rate in the peak regions of Fig. 7.1.

7.2 Comparison of active and passive MCP filter measurements

A similar phase effect as for the passive MCP filter measurements can be observed in Fig. 7.2. But in contrast to that, there are now count rate dips, where there were count rate peaks for the passive measurements of Fig. 7.1. Additionally, the constant background noise of a few $\mathrm{cts/s}$ for Fig. 7.1 is for the active measurements in the area of $400\,\mathrm{cts/s}$ (see Fig. 7.2). In this elevated constant count rate region, one can assume that nearly every single electron generates secondaries. This statement is supported by the measurements from Fig. 7.3, where the constant count rate region of the active MCP measurement is of the same magnitude like the maximum region of the one without any MCP filter in the beam line.
The count rate oscillations of Fig. 7.3 for the case without any MCP filter in beam line stem from the fact, that the MCP detector is also subject to a phase effect as it is the case for the MCP filter (see Section 6.1). Against this, the active MCP measurements do not underlie a phase effect in the constant count rate regions. This follows, because in this regions every detector count is induced by an avalanche of electrons, generated in the MCP-filter-wall-interaction. These multiple electrons have different gyrophases, when entering the MCP detector. It can therefore be assumed, that at least one of the multiple electrons gets multiplied within the MCP detector channels. Subsequently, no phase dependent effect is to be expected.
Considering this, we have to look at the constant count rate regions in order to asses the signal loss for the increased integration/differential time of $500\,\mathrm{ns}$ for the active MCP filter measurements. Via the count rate difference of $(40.5 \pm 29.9)\mathrm{cts/s}$ and the absolute background count rate of $(410.8 \pm 22.4)\mathrm{cts/s}$ from Fig. 7.3 we obtain a relative signal loss of $(9.7 \pm 7.0)\%$ (uncertainties originate from the constant fit uncertainties of Fig. 7.3). At a parallel single electron suppression value of $(80.5 \pm 7.9)\%$, we should therefore be able to separate most single electrons from

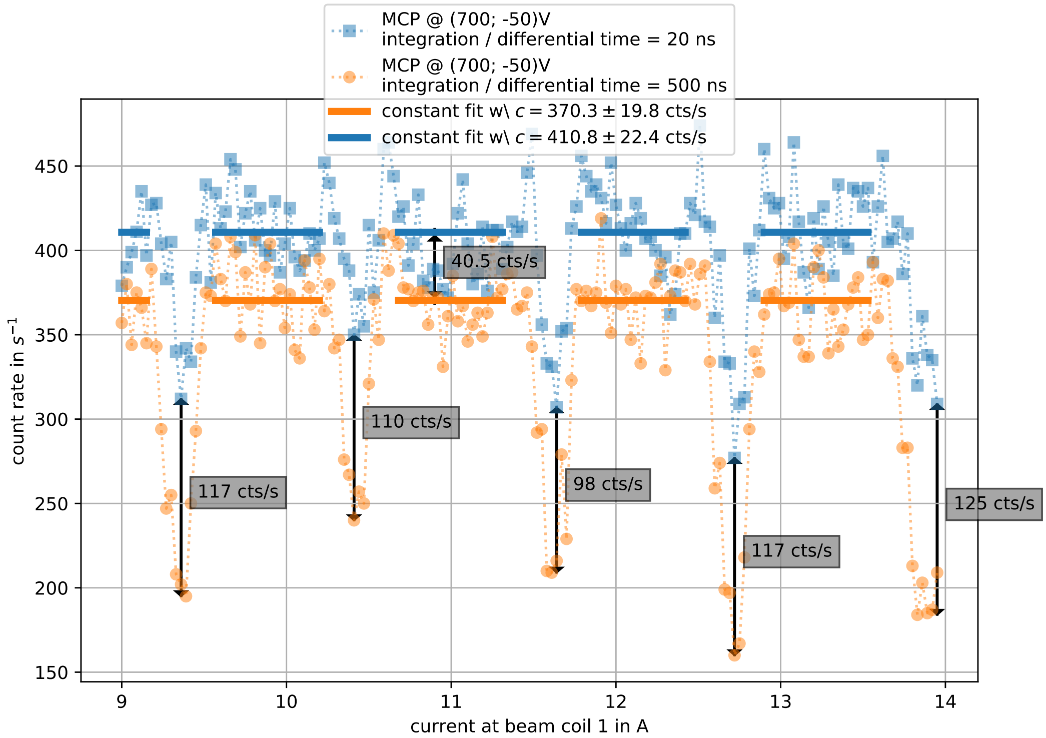

Figure 7.2.: Phase sensitive variation of the beam coil 1 current for the active MCP filter with an integration/differential time of $20\,\mathrm{ns}$ and $500\,\mathrm{ns}$ at the TFA, aiming for a bigger phase effect amplitude for higher integration/differential times. The MCP filter has been operated at a differential Voltage of $700\,\mathrm{V}$ and at a reference Voltage of $-50\,\mathrm{V}$ (MCP @ $(700; -50)\mathrm{V}$). Error bars smaller than symbols.

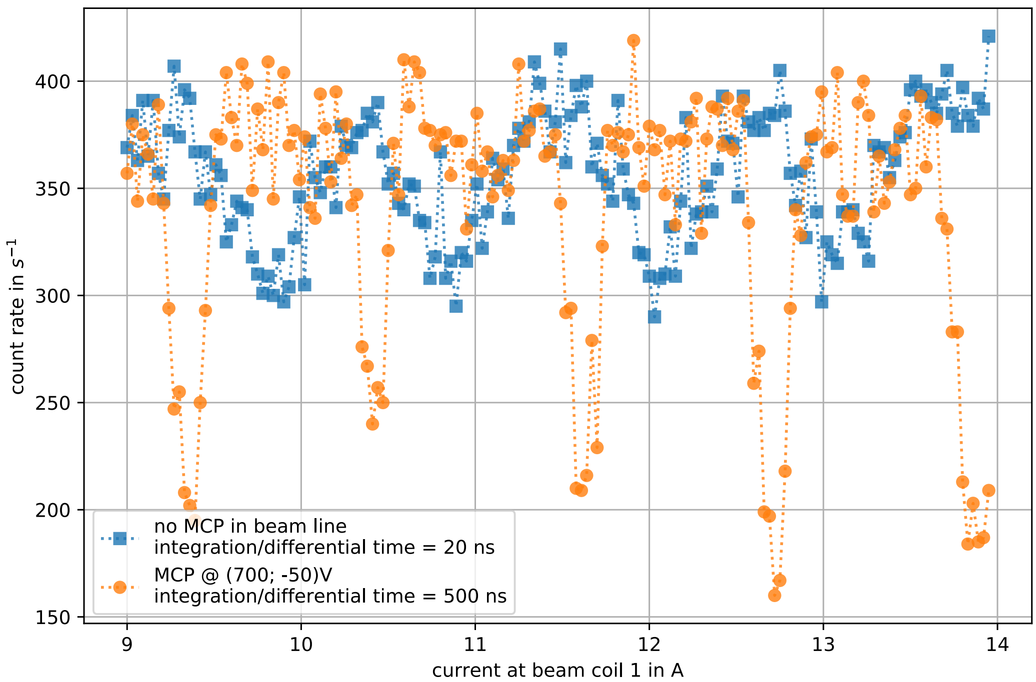

Figure 7.3.: Phase sensitive variation of the beam coil 1 current for the active MCP filter with an integration/differential time of $500\,\mathrm{ns}$ and for no MCP filter in beam line with an integration/differential time of $20\,\mathrm{ns}$. This plot shows a similar count rate in the peak regions of both measurements. Error bars smaller than symbols.

secondaries.
With more than $110\,\mathrm{cts/s}$ of count rate difference between the $500\,\mathrm{ns}$ and the $20\,\mathrm{ns}$ integration/differential time measurement in the region of minimums, the difference is significantly higher than the one of the background region with $(40.5 \pm 29.9)\mathrm{cts/s}$. This phenomenon hints to single electrons, which are able to pass the MCP filter at a certain current without channel-wall-interaction. It is to suppose that due to the single electron suppression most of these electrons do not get counted for an integration/differential time at the TFA of $500\,\mathrm{ns}$. The count rate difference of the passive MCP from Fig. 7.1 can help to further understand the effect. In this case, the count rate difference of Fig. 7.1 should be equivalent to the difference of count rate differences in the constant and the dip region of Fig. 7.2. Deviations may occure from discrepancies in the electro-magnetic field inside the MCP filter. While for the passive measurement the potential at the MCP front and back is equivalent, there is a $700\,\mathrm{V}$ potential difference between MCP front and back for the active measurements. This results in differing probabilities for electrons to pass the filter.
Another comment should relate to the count rate dips for the active MCP filter with an integration/differential time of $20\,\mathrm{ns}$ (see Fig. 7.2). In theory we would not expect dips here. For an integration/differential time of $20\,\mathrm{ns}$, every electron, either single or secondary electrons, should be counted at the pulse counter. One explanation for the divergence between theory and measurements, could be due to the OAR of the

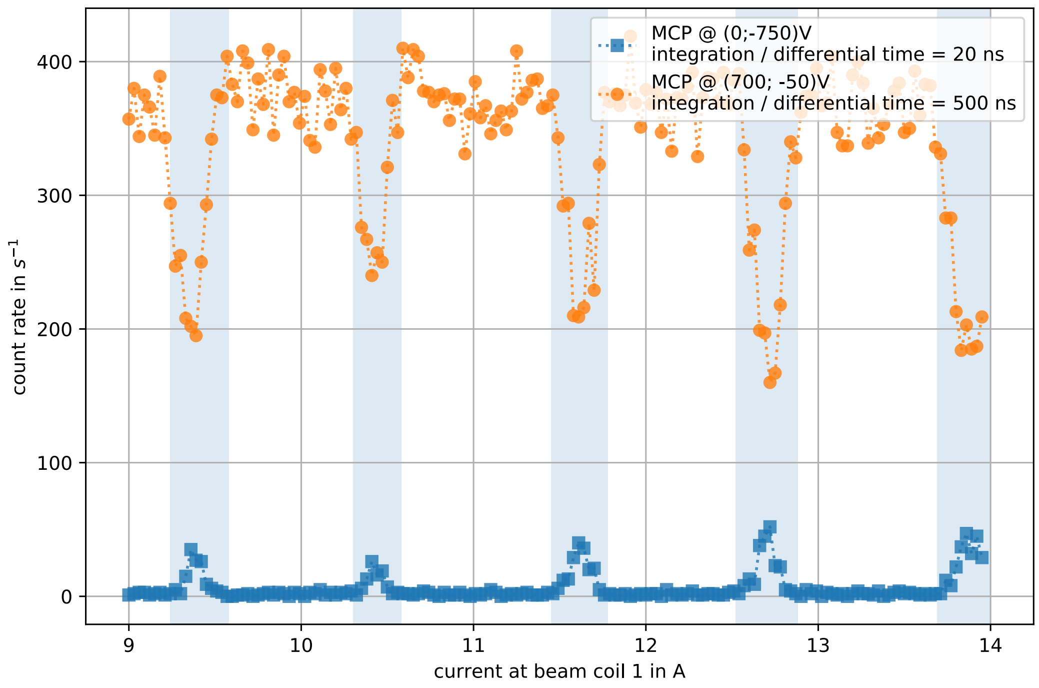

Figure 7.4.: Phase sensitive variation of the beam coil 1 current for the active and passive MCP filter with an integration/differential time of $500\,\mathrm{ns}$ and $20\,\mathrm{ns}$ at the TFA, showing that the gyrophases (beam coil 1 currents) of passive and active phase effect are in agreement (highlighted by the blue areas). Error bars smaller than symbols.

MCP detector. Assuming an OAR of $60\,\%$ as indicated in Section 3.2.2, leads to a $40\,\%$ decreased probability for a single electron to get detected in the MCP detector. For the electron avalanche, there is no such OAR restriction to be expected. It is to suppose, that at least one of the multiple electrons enters the MCP detector channels, thus producing a countable MCP detector pulse. Secondly the MCP detector phase effect (see Fig. 7.3) impacts the single electrons, so that for certain gyrophases not every single electron will be detected. Thirdly it is conceivable, that in the dip region electrons hit the MCP filter channel wall near the MCP back. This results in a lower or in even no multiplicity of electrons in the MCP filter for active measurements. Reason for this is the lower potential gradient near the MCP back, making it less probable for electrons to be released from the activation layer.

An alternative way to better understand the count rate dips, is to compare the dip positions of the active and the passive MCP filter measurements. In Fig. 7.4 one can find the peak positions of the passive MCP filter at about the same beam coil 1 current like the dips of the active MCP filter measurement. Assuming that all electrons see the same electric counter field before entering the MCP filter, either for the passive or active MCP filter, ensures identical gyrophases for equal beam coil 1 currents (for a detailed description of the beam coil 1 current dependency on the gyrophase, see Section 6.2). From this it can be concluded, that the dips of the active MCP filter measurements originate from the same phase effect observed at the passive MCP measurements from Chapter 6. Fig. 7.4 therefore illustrates, that the active MCP filter works as an inverted passive MCP filter.

In summary, the comparison between active and passive MCP filter measurements has proven the successful separation between secondary electrons, generated in MCP-channel-wall-interactions, and single electrons that passed the MCP filter.

8 Summary and Outlook

In this work the working concept of an aTEF has been verified. By investigation of the electron multiplication that enables the distinction between background and beta electrons, a filtering of the Rydberg induced background electrons with smaller gyroradii can be achieved.

Since the development of an aTEF is still ongoing, we have chosen an MCP for the conducted measurements. The MCP as well as the aTEF feature an SEE layer, generating secondary electrons in the order of 10^3 to 10^5 for incoming signal electrons that hit the channel wall [16]. Presuming a reduced wall hit probability for Rydberg electrons that have smaller gyroradii than most of the beta electrons at KATRIN, the aim was in this work to count the generated secondaries as one event, while suppressing single electron incidences at the detector.
For the purpose of testing the separation of secondary and single electrons, we used the aTEF test setup in Münster. This setup is featured with an Egun, an MCP filter in the center and an MCP detector at the end of the beam tube, able to register single electron events. Because the MCP channels are arranged with a bias angle, undesired for our measurement purpose, one had to determine the exact direction of the channels and adjust them analogously before the MCP was built into setup. Therefore the laser setup discussed in Chapter 5 has proven to be a suitable alignment method, that makes use of the interference pattern induced by a red laser. Yet the method is unable to manage a highly accurate adjustment, if just the zero order maximum is examined. For a more precise knowledge of the channel direction, higher orders of the interference pattern and its symmetry in best possible alignment configuration, would have to be taken into account.
By means of Monte Carlo simulations, it could be demonstrated that a slight deviation from the desired channel direction leads to a transmission probability depending on the phase of the cyclotron motion (gyrophases) the electron is performing in the aTEF setup. This phase effect also appeared during measurements, after the MCP was successfully built in, but still operated without SEE. An inverted phase effect at equal gyrophases could be identified, once the SEE layer of the MCP filter was active.
The appearance of both, the phase effect for passive and the inverted phase effect for active measurements, show that a distinction between secondary and signal electrons is possible and confirms the theoretical assumptions incorporated into the

simulation. These assumptions imply knowledge of the electron propagation inside the MCP channels, as well as knowledge about the SEE functionality for an active MCP.

In fact, an aTEF, which is intended to work similar to the used MCP but with differing dimension and material, could have the theoretical assumed properties, and therefore serve as a suppressor for Rydberg electrons. Even though this work did not investigate the properties of an actual aTEF, it hints, that the aTEF is a good approach towards the $0.2\,\mathrm{eV}$ sensitivity target of KATRIN in case the Rydberg hypothesis proofs to be correct.
Additionally, this thesis has shown, that a highly accurate alignment method is indispensable, if the aTEF will be installed within the KATRIN beam line one day.

Appendix A

A.1 Programming code for the Monte Carlo simulation of passive MCP filter measurements

Listing A.1: Class that determines the properties of the MCP and will be used in the `track_particle` function of Listing A.2 (Python3).

```python
#package that is required to execute the class MCP and the track_particle function
%pylab inline --no-import-all

class MCP:

    tan60 = np.tan(np.deg2rad(60))

    def __init__(self, Channel_dia, bias_angle, Channel_depth):
        """
        Initialising of the MCP

        :param Channel_dia: float like, the channel diameter of the MCP in micro meters
        :param bias_angle: float like, the bias angle of the MCP in micro meters
        :param Channel_depth: float like, the depth of the channels of the MCP in micro meters
        """
        self.Channel_dia = Channel_dia
        self.bias_angle = bias_angle
        self.Channel_depth = Channel_depth
        self.b = 0.5*self.Channel_dia
        self.a = self.b/(np.cos(np.deg2rad(self.bias_angle)))

    def creates_ellipses(self, step):
        """
        Creates ellipses of the cross section of the MCP in different depths = step

        :param step: float like, z-component of the observed ellipse in the MCP system

        :return: corners (array like [x, y, z])
        """

        x_offset = step*np.sin(np.deg2rad(self.bias_angle))
        z_offset = step*np.cos(np.deg2rad(self.bias_angle))
        corners = [[self.a*np.cos(np.deg2rad(angle))+x_offset, self.b*np.sin(np.deg2rad(angle)), z_offset] \
            for angle in range(0, 360, 1)]

        return corners

    def give_coordinates(self, step):
        """
        Creates the coordinates of the the ellipses at indicated step-depths so that every independent
        component has its own array.

        :param step: float like, z-component of the observed ellipse in the MCP system

        :returns: x (array like: []), y (array like: []), z (array like: [])
        """

        x = np.array([self.creates_ellipses(step)[i][0] for i in \
            range(0,np.shape(self.creates_ellipses(step))[0],1)])
        y = np.array([self.creates_ellipses(step)[i][1] for i in \
            range(0,np.shape(self.creates_ellipses(step))[0],1)])
        z = np.array([self.creates_ellipses(step)[i][2] for i in \
```

```
            range(0,np.shape(self.creates_ellipses(step))[0],1)])

        return x, y, z

    def tilting_MCP(self, tilt_angle, x, y, z, step = 0, given_coordinates = False):
        """
        Rotates the MCP coordinates at indicated step depths around the y-axis = tilting. If
        given_coordinates = True, one can as well rotate own coordinates.

        :param tilt angle: float like, the angle of the rotation around the y-axis in degrees
        :param  x ,y ,z : arrays like, arrays that shall be rotated if give_coordinates = True
        :param given_coordinates: boolean like, if given_coordinates = False the program takes the generated
                                            coordinates from step position

        :returns: x_ (array like: []), y_ (array like: []), z_ (array like: [])
        """
        x,y,z = x,y,z if given_coordinates else self.give_coordinates(step)

        x_ = x*np.cos(np.deg2rad(tilt_angle))+z*np.sin(np.deg2rad(tilt_angle))
        y_ = y
        z_ = -x*np.sin(np.deg2rad(tilt_angle))+z*np.cos(np.deg2rad(tilt_angle))

        return x_, y_, z_

    def rotation_MCP(self, rotation_angle,step, x_in = None, y_in = None, given_coordinates = False):
        """
        Rotates the MCP coordinates at indicated step depths around the z-axis = rotating. If
        given_coordinates = True, one can as well rotate own coordinates.

        :param rotation_angle: float like, the angle of the rotation around the z-axis in degrees
        :param  x ,y : arrays like, arrays that one like to rotate if give_coordinates = True
        :param given_coordinates: boolean like, if given_coordinates = False the program takes the coordinates
                                            from step position

        :returns: x_(array like: []), y_ (array like: [])
        """

        if given_coordinates:
            x, y = x_in, y_in
        else:
            x, y = self.give_coordinates(step)[0:2]

        b = np.deg2rad(rotation_angle)
        x_ = x*np.cos(b)-y*np.sin(b)
        y_ = x*np.sin(b)+y*np.cos(b)

        return x_,y_

    def inverse_rotation_MCP(self, x, y, rotation_angle):
        """
        Rotates the MCP coordinates at indicated step depths around the z-axis in inverse
        direction  = inverse rotating. If given_coordinates == True, one can as well rotate own coordinates.

        :param rotation_angle: float like, the angle of the rotation around the z-axis in degrees
        :param  x ,y : arrays like, arrays that one like to rotate if give_coordinates = True
        :param given_coordinates: boolean like, if given_coordinates = False the program takes the coordinates
                                            from step position

        :returns: x_ (array like: []), y_ (array like: [])
        """

        b = np.deg2rad(rotation_angle)
        x_ = x*np.cos(b)+y*np.sin(b)
        y_ = -x*np.sin(b)+y*np.cos(b)

        return x_,y_

    def excludes(self, x_test, y_test,  z_test, rotation_angle, hits = None):
        """
        Checks if positions went out of the rotated MCP. Keep in mind that the MCP will not be tilted in
        that function. For reasons of simpler calculations, it is always the electron beam, that will be
        tilted in the track_particle function.
        Then the function checks, wether the coordinates lie inside the MCP.
        If optional array with previous hits is given,
        returns updated array where additional outliers are also set to True.
        When the Point lies inside the  again, this value is NOT updated.

        :param x_test: array like, x-coordinates to check
        :param y_test: array like, y-coordinates to check
        :param rotation_angle: float like, the angle of the rotation around the z-axis in degrees
```

```
        :param hits: optional, array like, true / false values

        :returns res: boolean array whether points lie outside MCP or were outside before
        """

        if hits is None:
            res = np.zeros_like(x_test, dtype=bool)
        else:
            res = np.array(hits, dtype=bool)

        res += ~self.is_inside(x_test, y_test, z_test, rotation_angle,create_starters=False)

        return (res > 0)


    def is_inside(self, x_test, y_test, z_test, rotation_angle, create_starters = False, tilt_angle = 0):
        """
        Checks if given coordinates lie inside the MCP. Therefore the z-component is needed.
        This function can for the creation of the starting point (create_starters = True) as well check the
        condition at a certain tilt_angle.

        :param x_test, y_test, z_test: array like, x/y/z-coordinates to check
        :param rotation_angle: float like, the angle of the rotation around the z-axis in degrees
        :param create_starters: boolean like, if True the function checks the possible start positions
        :param tilt angle: float like, the angle of the rotation around the y-axis in degrees

        :return inside: boolean array whether points lie inside MCP
        """

        inside = np.zeros_like(x_test, dtype=bool)

        x_test_,y_test_=self.inverse_rotation_MCP(x_test,y_test,rotation_angle)
        x_test_-=z_test/np.tan(np.pi/2-np.deg2rad(self.bias_angle))

        #for modified tilt angle, the large half side of the ellipse (from the electron perspective) changes
        if create_starters == True:
            a = self.a*(np.cos(np.deg2rad(tilt_angle)))
            inside += ((x_test_**2/a**2 + y_test_**2/self.b**2) < 1)
        else:
            inside += ((x_test_**2/self.a**2 + y_test_**2/self.b**2) < 1) | (z_test >0) \
                | (z_test <-self.Channel_depth)

        return (inside > 0)

    def area_MCP_entry(self, tilt_angle, rotation_angle):
        """
        Calculates the area of the entry ellipse in the electron-system

        :param tilt angle: float like, the angle of the rotation around the y-axis in degrees
        :param rotation_angle: float like, the angle of the rotation around the z-axis in degrees

        return area: float like
        """

        x_data=np.array([self.a,0.0])
        y_data=np.array([0.0,self.b])

        x_data,y_data=self.rotation_MCP(rotation_angle, 0, x_data, y_data, given_coordinates=True)

        x_data,y_data=self.tilting_MCP(tilt_angle,x_data, y_data, np.array([0,0]), step=0, \
            given_coordinates=True)[0:2]

        return np.prod(np.sqrt(x_data**2+y_data**2))*np.pi
```

Listing A.2: Function, that tracks particles moving on a *gyro* track through a tilted and rotated MCP and checks wether these particles have hit the MCP wall (for a more detailed description see Chapter 4). This function calls up other functions from the `class MCP` of Listing A.1 (Python3).

```
def track_particle_MCP(MCP = MCP, num = 10000, angle_deg = 0.5, phase_set = False, \
    phase = 0, rotation_angle = 0, tilt_angle = 0, \
    starting_points = (None,None), given_angles = None, print_parameters = True):
    """
    Check the portion of signal electrons that won't produce any secondary electrons inside the tilted and
    rotated MCP.
    Plus, the electron beam density is invariant within the rotation or tilting. Means, relative intensity
    values of non-secondary electrons are comparable thru out the rotation/tilting.
```

```
    param MCP:           class ,    define the parameters of the MCP (diameter , bias angle , depth)

    param num:           integer , indicates the amount of electrons , which were guided through the channels

    param angle_deg:     float ,    represents the angle between magnetic field and the single electrons . It is
                         therefore an indicator of the transverse energy and determines the gyro radii

    param phase_set:     boolen , if True , there is no random phase spread within the electrons . All electrons
                         will start with the same phase = phase .

    param phase:         float ,    represents the phase of all electrons , if phase_set = True

    param rotation_angle:float ,    the angle the MCP will be rotated around the y-axis = rotating

    param tilt angle:    float ,    the angle  the MCP will be rotated around the y-axis in degrees = tilting

    param starting_points:        tuple of 1d-arrays of num-size , indicates the starting positions of the
                                                                   electrons if they don't change during
                                                                   different simulations

    param given_angles            1d-arrays of num-size ,          indicates the starting angles of the
                                                                   electrons if they don't change during
                                                                   different simulations

    param print_parameters:       boolean ,                        if set to True the used gyro_radii , the
                                                                   period length and the duration of the main
                                                                   iteration step will be printed

    :return:: non-secondary electron portion (float between 0 and 1)
    :return:: non-secondary electron portion normalised to the biggest possible area of the entry ellipse
              (float between 0 and 1) (makes different tilt angle measurements comparable)
    :return:: starting_points (tuple of 1d arrays of the used starting positions of the electrons)
    :return:: staring_angles (1d array of the used starting angles)
    """

    #initialising of parameter:
    B_det = 0.05 #B-field strength at the Egun in [T]
    E_0 = 1000 #electron energy once it was emitted from the Egun in [eV]
    D_STEP = 0.5 #step depths between the interfaces in [micro meter]

    if np.any(given_angles) != None:
        angle = given_angles
    else:
        angle = np.deg2rad(np.array([abs(angle_deg)]))

    ang = np.random.choice(angle,num)

    if np.any(starting_points[0]) != None:
        xs, ys = starting_points
    else:
        # generate start positions
        xs = []
        ys = []
        xs_plot = []
        ys_plot = []
        x1, y1 = MCP.rotation_MCP(rotation_angle = rotation_angle, step = 0, x_in = None, y_in = None, \
            given_coordinates = False)
        for _ in range(num):
            inside = False
            while (not inside):
                #creating coordinates, checking wether the starting position condition is fulfilled
                x_start = np.random.uniform(np.min(x1),np.min(x1)+2*MCP.a)
                y_start = np.random.uniform(np.min(y1),np.min(y1)+2*MCP.a)
                inside = MCP.is_inside(x_start,y_start,0,rotation_angle, create_starters=True, \
                    tilt_angle=tilt_angle)
            xs.append(x_start)
            ys.append(y_start)

        xs = np.array(xs)
        ys = np.array(ys)
    starting_points=(xs,ys)

    #initialising of the electro-magnetic environment which is directly connected with the electron track

    m_e = 9.1093837015*10**(-31)
    e = 1.602176634*10**(-19)
    E = E_0*e

    r_gyro = m_e*np.sin(ang)*(2*E/m_e)**(0.5)/(e*B_det)*1e6
```

```
    period_length = 2*np.pi*m_e*np.sqrt(2*E/m_e)/(e*B_det*np.cos(angle))*1e6

    phi = np.random.uniform(0, 2*np.pi,num) if (phase_set==False) else np.deg2rad(phase)

    # generate start positions with respect of the starting phase
    x0 = xs-r_gyro*np.cos(phi)
    y0 = ys-r_gyro*np.sin(phi)

    #initialises the z-component of the starting points. d != 0, because of the MCP is tilted, there can be as
    #well hits at z>0
    d = -int(MCP.b)
    hits = np.zeros_like(xs)


    #iteration steps adjusting the electron position and checking wether the new positions are still inside
    #the MCP.
    #Actually, the MCP will not be tilted, but the electron beam. But that makes no difference for the
    #calculations, except the sign of the indicated tilt angle
    while d < MCP.Channel_depth + int(MCP.b):
        d += D_STEP
        # the if condition intercepts the case of gyro radii equals 0
        delta_phi = d*e*B_det/(np.cos(ang)*(2*E/m_e)**(0.5)*m_e*1e6) if (np.any(r_gyro > 0)) else r_gyro
        xs = x0+r_gyro*np.cos(phi+delta_phi)
        ys = y0+r_gyro*np.sin(phi+delta_phi)
        xs_tilted, ys_tilted, zs_tilted = MCP.tilting_MCP(tilt_angle, xs, ys, np.array([-d]), step = 0, \
            given_coordinates=True)
        hits = MCP.excludes(xs_tilted, ys_tilted, zs_tilted, rotation_angle, hits)
        #interrupts the loop, if every electron hit the wall
        if np.sum(hits) == num:
            break

    #defines the results
    relative_non_hits = 1-np.sum(hits)/num
    # makes the results comparable, means to standardise the electron production per area
    standardised_non_hits = (1-np.sum(hits)/num)*(MCP.area_MCP_entry(tilt_angle,rotation_angle)/ \
        MCP.area_MCP_entry(MCP.bias_angle,0))

    #prints specefications of electron track
    if print_parameters == True:
        print("gyro radii", r_gyro[0])
        print("period length", period_length[0])
        print("relative hits (np.sum(hits)/num): ", np.sum(hits)/num)

    return relative_non_hits, standardized_non_hits
```

Acronyms

AP Analysing Plane

aTEF active Transverse Energy Filter

CAD Computer-Aided Design

Egun mono energetic electron source

FPD Focal Plane Detector

KATRIN Karlsruhe Tritium Neutrino experiment

KIT Karlsruhe Institut of Technology

MAC-E Magnetic Adiabatic Collimation with Electrostatic

MCP Microchannel Plate

OAR Open Area Ratio

SAP Shifted Analysing Plane

SEE Secondary Electron Emission

SM Standard Model of particle physics

TEF Transverse Energy Filter

TFA Timing Filter Amplifier

UHV Ultra High Vacuum

WGTS Windowless Gaseous Tritium Source

Bibliography

B

[1] N. Trost. „Modeling and measurement of Rydberg-State mediated Background at the KATRIN Main Spectrometer“. PhD thesis. Karlsruher Institut für Technologie (KIT), 2019. URL: https://publikationen.bibliothek.kit.edu/1000090450.

[2] J. D. Behrens. „Design and commissioning of a mono-energetic photoelectron source and active background reduction by magnetic pulse at the KATRIN experiment“. PhD thesis. Westfälische Wilhelms-Universität Münster (WWU), 2016. URL: https://www.uni-muenster.de/imperia/md/content/physik_kp/agweinheimer/theses/phd-behrens.pdf.

[3] L. Schimpf. „Characterisation of energy loss processes of 18.6 keV electrons inside the windowless tritium source of KATRIN“. PhD thesis. Karlsruher Institut für Technologie (KIT), 2021. URL: https://publikationen.bibliothek.kit.edu/1000131810.

[4] F. M. Fränkle et al. „KATRIN background due to surface radioimpurities“. In: (2020). arXiv: 2011.05107 [physics.ins-det].

[5] E. Fermi. „Versuch einer Theorie der -Strahlen. I“. In: *Zeitschrift für Physik* 88 (3-4 1934), pp. 161–177. DOI: 10.1007/BF01351864.

[6] J. Angrik et al. *KATRIN Design Report 2004*. 2005. DOI: 10.5445/IR/270060419.

[7] M. Aker et al. „First direct neutrino-mass measurement with sub-eV sensitivity“. In: (2021). arXiv: 2105.08533 [hep-ex].

[8] M. Aker et al. „The Design, Construction, and Commissioning of the KATRIN Experiment“. In: (2021). arXiv: 2103.04755 [physics.ins-det].

[9] R. G. H. Robertson. „Transverse Energy Filter“. Report. University of Washington, Seattle, 2019.

[10] A. Lokhov. „KATRIN experiment: recent results and future prospects“. In: (Dec. 3, 2020). Talk on the KAT Strategy Meeting.

[11] A. Fulst et al. „Time-focusing time-of-flight, a new method to turn a MAC-E-filter into a quasi-differential spectrometer“. In: *The European Physical Journal C* 80.10 (2020). DOI: 10.1140/epjc/s10052-020-08484-9.

[12] K. Gauda. „Investigation of Transverse Energy Filter Configurations“. In: (Sept. 10, 2020). Talk on the 39$^{\text{th}}$ KATRIN Collaboration Meeting.

[13] R. Salomon. „Development of a Setup to test Time-Of-Flight Methods for the KATRIN Experiment“. Bachelor’s thesis. Westfälische Wilhems-Universität Münster (WWU), 2019. URL: https://www.uni-muenster.de/imperia/md/content/physik_kp/agweinheimer/theses/bachelor-richard_salomon.pdf.

[14] J. Behrens et al. „A pulsed, mono-energetic and angular-selective UV photoelectron source for the commissioning of the KATRIN experiment“. In: *European Physical Journal C* 77 (2017). DOI: 10.1140/epjc/s10052-017-4972-9.

[15] A. U. Mane et al. „A novel atomic layer deposition method to fabricate economical and robust large area microchannel plates“. In: *Micro- and Nanotechnology Sensors, Systems, and Applications III* 8031 (2011), 80312H. DOI: 10.1117/12.882885.

[16] A. U. Mane et al. „An Atomic Layer Deposition Method to Fabricate Economical and Robust Large Area Microchannel Plates for Photodetectors“. In: vol. 37. Elsevier B.V., 2012, pp. 722–732. DOI: 10.1016/j.phpro.2012.03.720.

[17] tectra GmbH. *MCP-50-D-L-A-F Catalog*. tectra GmbH. Reuterweg 51-53, Frankfurt a.M., 2019.

[18] P. Oelpmann. „master thesis in preparation“. MA thesis. Westfälische Wilhems-Universität Münster (WWU), 2021.

[19] Ulrich Stroth. *Plasmaphysik*. Springer Berlin Heidelberg, 2018, pp. 15–18. ISBN: 978-3-662-55236-0.

[20] K.-H. Goldhorn, H.-P. Heinz, and M. Kraus. *Moderne mathematische Methoden der Physik*. Springer Berlin Heidelberg, 2010, p. 148. ISBN: 978-3-642-05184-5.

[21] H. Knörrer. *Geometrie*. Vieweg, 2006, p. 160. ISBN: 978-3-8348-0210-1.

[22] W. Demtröder. *Experimentalphysik 2*. Springer Berlin Heidelberg, 2017, pp. 88, 315, 319, 335. ISBN: 978-3-642-29944-5.

[23] Wikipedia. *Zylinderspule*. URL: https://de.wikipedia.org/wiki/Zylinderspule (visited on 07/15/2021).

This Bachelorthesis was written with LaTeX using the template *gc-thesis* of Phil Steinhorst. See for more information https://github.com/phist91?tab=repositories.

Declaration of academic integrity

I hereby confirm that this thesis on "Simulations and measurements of angular selective electron transmission and detection for the KATRIN experiment" is solely my own work and that I have used no sources or aids other than the ones stated. All passages in my thesis for which other sources, including electronic media, have been used, be it direct quotes or content references, have been acknowledged as such and the sources cited.

26.07.2021, Münster

(place, date) (signature)

I agree to have my thesis checked in order to rule out potential similarities with other works and to have my thesis stored in a database for this purpose.

26.07.2021, Münster

(place, date) (signature)